Crustal Structure Beneath the Northern Appalachians and the Eastern Grenville Province

Omid Bagherpur Mojaver[1], Fiona Darbyshire[1]

[1]Centre de recherche Geotop, Université du Québec à Montréal

Key Points:

- Crustal thickness and velocities in eastern Canada are more variable in the Peri-Gondwanan than Peri-Laurentian domains
- A step-like Moho feature in the northern Appalachians marks the boundary between the Peri-Gondwanan and Peri-Laurentian domains at depth
- The lower crust in the Grenville Province is thicker and faster than that observed beneath the northern Appalachians

Corresponding author: Omid Bagherpur Mojaver, `omid.bagherpur@gmail.com`

Abstract

Southeastern Canada and the northeastern USA include terranes that were tectonized since the Archean, making this region an excellent place to investigate the evolution of continental crust. Our study area covers the Archean southeastern Superior Province, the Proterozoic eastern Grenville, and the Phanerozoic northern Appalachians comprising terranes with either Peri-Laurentian or Peri-Gondwanan heritage. Adopting a Rayleigh wave ambient noise tomography method, we used noise data recorded between 2013 and 2015, and obtained high resolution anisotropic tomographic images of the crust enabling us to discuss tectonic implications. The azimuthal anisotropy orientations follow a dominant NE-SW trend across the study area, but some localized changes of anisotropy direction in the Bay of Fundy and across the Appalachian front are observed. The crust beneath the older Superior and Grenville provinces is generally fast, whereas the Appalachians include strong slow anomalies, especially at upper crustal depths, where they represent thick sedimentary basins beneath the St. Lawrence valley, the Gulf of St. Lawrence and the Bay of Fundy. We suggest that the boundary between the Peri-Laurentian and the Peri-Gondwanan terranes at depth is marked by a Moho-offset feature observable in our models. A generally similar crustal seismic signature for the youngest two easternmost tectonic domains suggest that they were never separated by a wide ocean basin. Our results provide important evidence for evolution of the continental crust during and after accretionary/collisional episodes in the study area.

Plain Language Summary

Southeastern Canada and the northeastern USA comprise rocks that preserve the formation and evolution of continental crust over at least 2.5 billion years, making this region an ideal place to improve our understanding of the processes that created today's continents, such as rifting or mountain building. Seismic noise data recorded by a network of stations can be analysed to model crustal structure, using the speed at which seismic waves travel through the crust at different depths, and the resulting models help us to understand how the crust was formed and modified over geological time. We used more than two years of seismic noise datasets and measured the variations of seismic velocity structure in different crustal layers, as well as the total thickness of the crust across the study area. We observed that the younger crustal domains have a more complex upper layer structure than the older units. The older domains, however, have a faster and

thicker lower crustal layer than the younger zones. Beneath the central younger domains of the northern Appalachians, we observed that the crustal thickness varies over a short distance, creating a step-like geometry for the base of the crust.

Index Terms and Keywords

7205 – Continental crust, 7255 – Surface waves & free oscillations, 7270 – Tomography, 8103 – Continental cratons, 8108 – Continental tectonics: compressional

1 Introduction

Eastern North America is an important place to investigate the implication of the theory of plate tectonics. This is due to geological units in this area preserving a protracted history of formation and evolution for ages varying from Archean to Phanerozoic. Discussing tectonic implications for such a complex region requires a deep understanding of the crustal structure. To this end, seismic tomography models are extremely valuable as they can provide us with a detailed look at the velocity structure at different scales. With the aim of obtaining high resolution tomographic images of the crust and sub-Moho structure beneath southeastern Canada and the NE United States, we used recent records of broadband seismic data in a passive seismic technique, namely Ambient Noise Tomography (ANT; Shapiro & Campillo, 2004; Shapiro et al., 2005), that has been successful in recovering detailed crustal and uppermost mantle velocity structure in regional-scale (e.g., Green et al., 2017; Lin et al., 2008; McLellan et al., 2018; Kuponiyi et al., 2017; Pawlak et al., 2012; Y. Yang et al., 2008) and continental scale (e.g., Bensen et al., 2008; Kao et al., 2013; Y. Yang et al., 2007) studies. Recently added data coverage in our study area, in the years from 2013 to 2015, provides us with an unprecedented opportunity to recover the highest resolution anisotropic velocity structure of the crust and sub-Moho depths to date. We use our models along with previous geophysical constraints to discuss tectonic implications.

1.1 Tectonic setting

Our study area spans ∼3/4 of Earth's geological history with geological units that were formed and tectonized from Archean to Mesozoic. The three major tectonic provinces from the oldest to youngest are the Archean southeastern Superior Province, the Proterozoic eastern Grenville, and the Phanerozoic northern Appalachians.

In the far northwest of the study area, a small part of the southeastern Superior Province including the eastern Abitibi subprovince and the northeastern Pontiac domain are covered by this study. These tectonic domains comprise a collage of mafic to felsic volcanic units with ages ranging from 2750 Ma to 2690 Ma (e.g., Ludden & Hynes, 2000). The Grenville front marks the NW limit of the Grenvillian metamorphism and deformation, and separates the Superior from the eastern Grenville Province (e.g., Rivers et al., 1989). The Grenville Province arises from a ∼300 Ma period of accretions and orogenesis coinciding with the final assembly of the supercontinent Rodinia at ∼1 Ga (Whitmeyer & Karlstrom, 2007). Based on deformation, metamorphism, and geophysical contraints, the eastern Grenville orogen is divided into three first order belts including Parautochthonous Belt (PB), Allochthonous Monocyclic Belt (AMB), and Allochthonous Polycyclic Belt (APB) (e.g., Rivers, 2008). In the northwest of the Grenville, sub-parallel to the Grenville front, the PB is associated with high pressure and temperature Grenvillian metamorphism representing a section of exhumed Laurentian crust overlying a southeast dipping parautochthonous Archean basement (e.g., Rivers, 2015). The AMB consists of exotic terranes accreted to Laurentia between 1080 and 1035 Ma (Carr et al., 2000). The APB covers the majority of the Grenville Province and comprises terranes originally part of a Laurentian continental margin arc setting and preserves evidence of Paleoproterozoic to early Mesoproterozoic metamorphism overprinted by metamorphism of Grenvillian age (Rivers et al., 2002). The Grenvillian orogeny occured in two phases, namely Ottawan and Rigolet phases (Rivers, 2015; Darbyshire et al., 2017). The Ottawan orogenic phase (∼1090-1020 Ma) is restricted to the Allochthonous terranes and characterized by a high grade metamorphic signature, and a period of significant crustal shortening and thickening resulting in formation of an orogenic plateau. The relatively long-duration Ottawan phase was followed by the much shorter (∼1005–980 Ma) Rigolet phase that was restricted to the Parautochthonous terranes along the hanging wall of the Grenville front.

The Appalachian front is a first order structural boundary separating the Grenville Province from the northern Appalachians. The northern Appalachians were tectonized during four orogenic episodes occurring from 485 to 350 Ma (C. R. van Staal et al., 2009, 2012). Accretion of terranes during these orogenic episodes coincided with rift-drift processes associated with the opening and closing of the Iapetus and Rheic oceans (Hibbard, van Staal, & Miller, 2007). Tectonic domains in the northern Appalachians from west

to east (i.e., oldest to youngest) are the Humber margin, Dunnage zone, Ganderia, Avalonia, and Meguma. Terranes belonging to these domains have either Gondwanan or Laurentian provenance. Accretion of the terranes currently situated in the Humber margin and the Dunnage zone occurred during the Taconic orogeny (485–450 Ma; C. R. van Staal & Barr, 2012). The Humber margin extends along the eastern edge of the Appalachian front and records opening of a Taconic seaway and the Iapetus ocean at 615 Ma (S. L. Kamo et al., 1989; Hibbard, van Staal, & Rankin, 2007). The Dunnage zone comprises intra-oceanic terranes originally belonging to Gondwana or Laurentia with a faulting system, named Red Indian Line, seperating the Gondwanan and Laurentian units (Williams et al., 1988; Macdonald et al., 2014). The three coastal domains of the northern Appalachians, namely Ganderia, Avalonia, and Meguma, include Peri-Gondwanan realms that accreted to eastern Laurentia during three different orogenic episodes: the Salinic (450–423 Ma), Acadian (421–400 Ma), and Neo-Acadian (395–350 Ma) (C. R. van Staal et al., 2009, 2012; Levin et al., 2017). Ganderia was rifted from Gondwana in the late Neoproterozoic and accreted to eastern North America in the late Ordovician to early Silurian closing the Iapetus ocean (C. R. van Staal et al., 2012; Wilson et al., 2017). Avalonia was accreted to the Ganderia passive margin during the late Silurian to early Devonian Acadian orogeny. Lastly, accretion of Meguma to eastern north America occurred during the middle Devonian to early Carboniferous Neo-Acadian orogeny. The northern Appalachian orogenesis was terminated by collision of Gondwana and composite Laurentia in the Carboniferous-Permian Alleghanian orogeny resulting in the formation of supercontinent Pangea (C. R. van Staal & Barr, 2012). Accretion-related structures in the present-day northern Appalachians have escaped from Alleghanian modifications as the suture zone was far, and is now concealed in the margins of the Atlantic ocean (C. R. van Staal & Barr, 2012). Accordingly, pre-Alleghanian tectonic history in the northern Appalachians is mostly well preserved.

The Canadian Appalachians have been tectonically quiet since the Cretaceous, and the latest tectonic activity was during the breakup of Pangea resulting in development of the Eastern North American rift systems that include the Fundy basin (Withjack et al., 2009). The formation of the Bay of Fundy was due to orogen-perpendicular (NW-SE) rifting that started in the Middle Triassic, which also activated NE trending compressional structures as normal faults (Withjack et al., 1995). Rifting ceased in the Bay

139 of Fundy when Early to Middle Jurassic continental breakup led to the opening of the

140 North Atlantic ocean (Funck et al., 2004; Withjack et al., 2009).

1.2 Previous seismic studies

142 Thanks to the Lithoprobe project in the 1990s (e.g., Clowes, 2010) and installa-

143 tion of temporary broadband seismographs in the last ∼20 years (e.g., Eaton et al., 2005),

144 seismology has significantly improved our understanding of the structure of eastern Canada

145 at crustal and uppermost mantle depths. Seismic structure in different parts of our study

146 area has been investigated at different scales and depth ranges using various techniques

147 including ambient noise tomography (e.g., Kuponiyi et al., 2017; Kao et al., 2013; Bensen

148 et al., 2009), earthquake-based tomography (e.g., Shen & Ritzwoller, 2016; Petrescu et

149 al., 2017; Schaeffer & Lebedev, 2014; Bagherpur Mojaver et al., 2021; Boyce et al., 2016),

150 joint inversion of seismic ambient noise and earthquake data (Golos et al., 2018), receiver

151 function methods (e.g., Petrescu et al., 2016; Levin et al., 2017; Li et al., 2018, 2020),

152 shear wave splitting measurements (e.g., Darbyshire et al., 2015; Gilligan et al., 2016;

153 Long et al., 2016; B. B. Yang et al., 2017), and reflection-refraction seismic profiling (e.g.,

154 Clowes, 2010; Cook et al., 2010; Hammer et al., 2010; Ludden & Hynes, 2000). In this

155 section we provide a brief review of the previous findings.

156 Using ambient seismic noise data, a few continental-scale studies modelled the seis-

157 mic structure of the crust and uppermost mantle in our study area (e.g., Kao et al., 2013;

158 Bensen et al., 2009). According to their models, seismic structure of the crust beneath

159 the northern Appalachians appears to be more complex than the Precambrian domains.

160 An interesting observation is a large velocity gradient recovered throughout different parts

161 of the Canadian shield at mid-crustal depths and up to about the Appalachian front, in-

162 terpreted as a relict rheological boundary between the upper and lower crust (Kao et al.,

163 2013). The Gulf of St. Lawrence at depths < 20 km is dominated by slow anomalies (Kao

164 et al., 2013). A regional-scale study carried out over this area suggests a maximum sed-

165 imentary thickness of ∼8 km beneath this region (Kuponiyi et al., 2017). It is also sug-

166 gested that the Grenvillian basement beneath the northern Appalachians is wedged out

167 at depth by the Red Indian Line (Kuponiyi et al., 2017). Adopting a probabilistic joint-

168 inversion scheme, Shen & Ritzwoller (2016) used receiver functions, group and phase ve-

169 locities from ambient noise and earthquakes, and Rayleigh wave ellipticity measurements,

170 and obtained high resolution shear velocity models at crustal and uppermost mantle depths
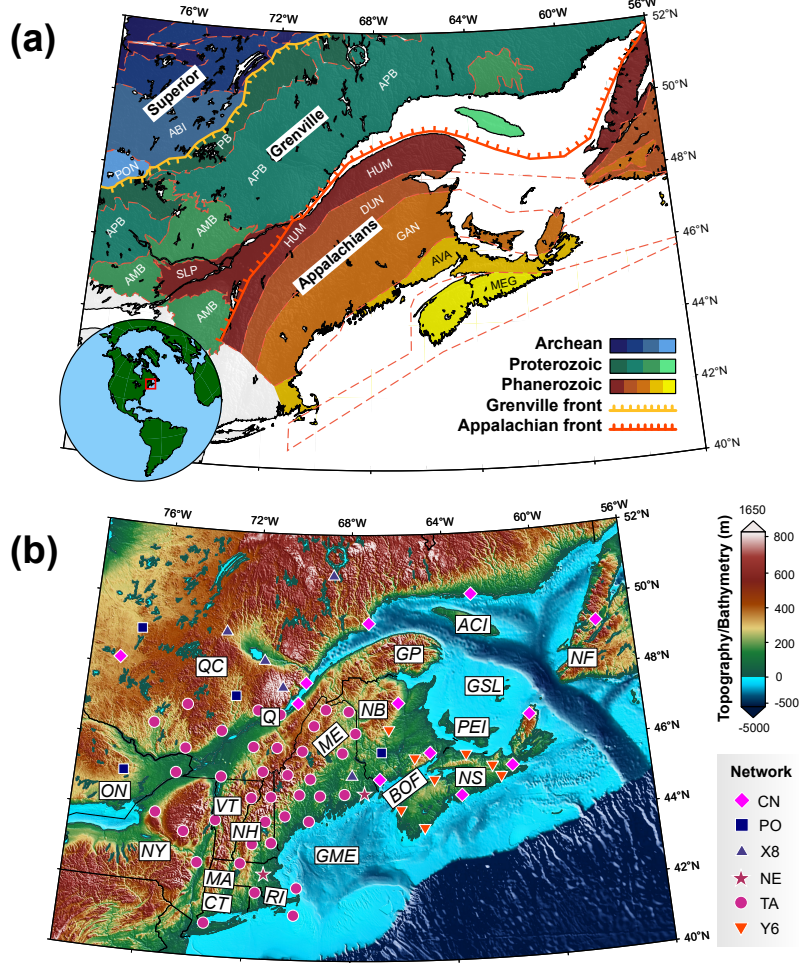
Figure 1. (a) Simplified tectonic map of eastern Canada. ABI: Abitibi subprovince, AMB: Allochthonous Monocyclic Belt, APB: Allochthonous Polycyclic Belt, AVA: Avalonia, DUN: Dunnage zone, GAN: Ganderia, HUM: Humber margin, MEG: Meguma, PB: Parautochthonous Belt, PO: Pontiac domain, SLP: St. Lawrence platform. (b) The 69 broadband seismic stations belonging to 6 seismograph networks overlain on topography/bathymetry of the study area. ACI: Anticosti Island, BOF: Bay of Fundy, CT: Connecticut, GME: Gulf of Maine, GP: Gaspé Peninsula, GSL: Gulf of St. Lawrence, MA: Massachusetts, ME: Maine, NB: New Brunswick, NF: Newfoundland, NH: New Hampshire, NS: Nova Scotia, NY: New York, ON: Ontario, PEI: Prince Edward Island, Q: Quebec City, QC: Quebec (province), RI: Rhode Island, VT: Vermont.

across the entire USA. A noteworthy observation of their final crustal thickness map is a ~8 km Moho depth contrast with NE-SW trend over a relatively small distance within the northern Appalachians.

Variations in crustal thickness and bulk crustal composition beneath our study area have been investigated through seismic methods of receiver functions (Levin et al., 2017; Petrescu et al., 2016), reflection-refraction seismic profiling (e.g., Cook et al., 2010), and surface wave tomography (e.g., Kao et al., 2013; Bagherpur Mojaver et al., 2021). Results from the reflection-refraction seismic profiles suggest that the Moho depths beneath our study area vary from ~30 km to 45 km (Ludden & Hynes, 2000; Hall et al., 1998). Available receiver function studies carried out over our study area suggest that the crustal thickness varies between ~25 and ~50 km, with more small-scale variations of crustal thickness and Vp/Vs ratio occurring beneath the Appalachians than the older Precambrian domains (Petrescu et al., 2016; Levin et al., 2017). These results also indicate that the greatest complexity of crustal properties (crustal thickness, Moho thickness, Vp/Vs ratio) occurs across the Appalachian front (Levin et al., 2017). Crustal and lithospheric thickness estimates from a previous surface wave study and active seismic profiles do not suggest a simple relation for the thickness of these layers with the age of the terranes, and a generally thinner crust and lithosphere is suggested beneath the central part of the Appalachians (Bagherpur Mojaver et al., 2021; Hall et al., 1998). Using receiver functions with broadband datasets spanning more than 20 years, a detailed look at the crustal structure of the Grenville and Appalachian provinces beneath the northeastern USA is presented by Li et al. (2018) and Li et al. (2020). They note crustal thickness variations roughly correlated with surface elevation and anticorrelated with Bouger gravity anomaly, sharp Moho steps with maximum offset of 15 km within narrow zones, and an eastward decrease of Moho thickness. These results are indicative of a very complex 3D crustal structure beneath our study region.

Among the reflection-refraction seismic profiles carried out during the Lithoprobe project, several profiles belonging to the Abitibi-Grenville transect (AG; lines 52, 53, and 54 in the Grenville Province; Ludden & Hynes, 2000), and the Lithoprobe-East transect (LE; lines 86/1, 86/2, 86/4, 86/5, and 88/1 in Gulf of St. Lawrence; Hall et al., 1998) lie within our study area. Although results from other profiles outside the study area are still useful (e.g., Newfoundland), we note that caution must be exercised in translating their conclusions into our study area. This is mainly because the Laurentian margin had

a very irregular shape before the Paleozoic accretionary events (Stockmal et al., 1987). The study of active seismic profiles in the Appalachians suggests that the Grenvillian basement is at least extended beneath the Humber margin and part of the Dunnage zone, and it is distinguished by strong mid-crustal reflectors, moderately strong lower crustal reflectors and relatively deep Moho depths (Hall et al., 1998). It is also suggested that the Superior craton continues as a wedge into the Grenville lower crust 200-300 km southeast of the Grenville front (Rivers, 1997; Ludden & Hynes, 2000). Interpretation of the Lithoprobe AG lines in the Grenville suggests that the southeast dipping reworked Archean basement is less extended beneath our study area compared to the farther southwest Lithoprobe profiles in the Grenville Province (Ludden & Hynes, 2000). It is suggested that the mafic intrusive unit in the eastern portion of the AMB domain is underlain by high pressure terranes at least down to the Moho discontinuity, whereas in the western AMB, where a different allochthon unit is observed at the surface, underlying crustal structures are interpreted as two layers of high pressure terranes underlain by another layer of SE dipping Laurentian Archean material that was reworked during the Rigolet phase (Ludden & Hynes, 2000). Interesting findings of the active seismic profiles in the Appalachians include a generally thinner crust beneath the central part of the orogen relative to the continental margin and the western domains, and high velocity lower crust beneath the profiles over the Gulf of St. Lawrence which requires a mafic composition (Hall et al., 1998).

Global (e.g., Schaeffer & Lebedev, 2013; Ritsema & Lekić, 2020) and continental-scale (e.g., Shen & Ritzwoller, 2016; Schaeffer & Lebedev, 2014; Clouzet et al., 2018) tomographic models suggest an overall faster Superior and Grenville Province relative to the Appalachians. Available regional-scale tomographic studies observe clear systematic differences of seismic signatures for the three major tectonic domains with typically decreasing lithospheric mantle velocities from the Archean Superior to the Phanerozoic Appalachians (e.g., Boyce et al., 2016). A regional-scale study suggests a two-stage lithospheric formation beneath the North American Craton (Petrescu et al., 2017). In the northern Appalachians, systematic differences are observed between the lithospheric seismic velocities of the Peri-Laurentian terranes and the Peri-Gondwanan terranes (Yuan et al., 2014; Bagherpur Mojaver et al., 2021). A NW-SE trend of slow anomalies crosscutting the three major tectonic domains in eastern Canada is interpreted as resulting from the passage of the Great Meteor Hotspot (GMH) during Mesozoic times (Boyce et

al., 2016; Villemaire et al., 2012). Spatially coincident with the passage of the GMH, a strong slow anomaly in the northern Appalachians (Northern Appalachian Anomaly; NAA) is observed at depths from 60 to 100 km (e.g., Golos et al., 2018; Bagherpur Mojaver et al., 2021). It is interpreted as resulting from either compositional changes caused by the GMH tectonism (e.g., Boyce et al., 2016; Villemaire et al., 2012), or due to a small-scale convection process (Menke et al., 2016).

Several studies have modelled seismic anisotropy beneath the broadband seismographs of the study area using shear wave splitting techniques (e.g., Darbyshire et al., 2015; Gilligan et al., 2016; B. B. Yang et al., 2017). Shear wave splitting measurements give integrated anisotropy information over a wide range of depths from the base of the mantle to the surface. The relatively large splitting times (> 1 s) suggest contribution of both lithosphere and asthenosphere (Darbyshire et al., 2015; B. B. Yang et al., 2017). Multiple layers of anisotropy are suggested beneath southeastern Canada and the northeastern USA (Long et al., 2016). A generally parallel to subparallel trend of the splitting directions relative to the tectonic trend, weak correlation with the direction of absolute plate motion, and observed complex and small-scale variations of the anistropy orientation and magnitude suggest a more significant role for the lithosphere compared to asthenosphere in our study area (e.g., Darbyshire et al., 2015; Gilligan et al., 2016). Another study carried out over the NE USA, however, suggests that the observed anisotropy is mostly from the upper asthenosphere (B. B. Yang et al., 2017). The role of the crust in the observed anisotropy across our study area is not discussed in the available shear wave splitting measurements. In this case, constraining seismic anisotropy using surface wave tomography techniques can shed light on this issue, and has the advantage of giving depth-dependent (period-dependent) information as opposed to the depth-averaged shear wave splitting measurements.

2 Data and Method

2.1 Data and Data Processing

The data used in this study are continuous vertical component seismograms belonging to 69 broadband stations from 6 different seismograph networks (Figure 1b). The seismic networks are the Canadian National Seismograph Network (CN; Geological Survey of Canada, 1989), New England Seismic Network (NE; ASL, 1994), USArray Trans-

portable Array (TA; IRIS Transportable Array, 2003), Portable Observatories for Litho-
spheric Analysis and Research Investigating Seismicity (PO: POLARIS; Eaton et al., 2005),
and QM-III experiment (X8 and Y8 networks; Menke et al., 2012; SEIS-UK, 2013). The
stations belonging to the TA and QM-III networks were only operational in 2013-2015,
and combined with the data from other networks during that period, they provide us
with the inter-station path coverage required to recover high-resolution seismic veloc-
ity models across the study area.

The data acquisition process was carried out for the available daily records of all
stations from August 1, 2013 to November 1, 2015 (823 days). Some daily records were
rejected due to instrument irregularities and data fragmentation issues, resulting in a vari-
able number of daily records from 362 to 823 days, with an average of 716 days, for the
stations. We followed the recommended procedure of Bensen et al. (2007) for data pro-
cessing, except for the temporal normalization step where we chose to apply one-bit nor-
malization instead of the running absolute mean normalization method (e.g., Shapiro
& Campillo, 2004; Shapiro et al., 2005; Yao et al., 2006). Accordingly, single station data
processing steps applied to the daily records include removing the data trend and mean,
resampling of time-series to a common sampling rate of 1 Hz, instrument response re-
moval, one-bit normalization to exclude the earthquake signals, and spectral whitening
to flatten the ambient seismic noise in the frequency domain (Bensen et al., 2007).

By stacking long-duration noise cross-correlation time series, the Empirical Green's
Functions (EGFs) will emerge (e.g., Shapiro & Campillo, 2004). The positive (causal)
and negative (acausal) parts of the EGFs represent waves travelling in opposite direc-
tions between the station pairs, and the same physics as that used in surface wave anal-
ysis can be applied to these dispersive wavetrains to extract phase velocity information
for the paths between the stations (e.g., Y. Yang et al., 2008). We calculated EGFs for
all possible station pairs, resulting in more than 2340 EGFs with the stack number vary-
ing from 81 to 823 days, and average stack number of 650 days. Since our study area is
located next to the Atlantic coast, the energies of the emerging wavetrains for the causal
and acausal signals are significantly different (Figure 2). This could cause bias in the mea-
surement of phase velocities from the noise correlation functions (e.g., Tian & Ritzwoller,
2015). To quantify the bias due to non-uniform noise distribution in our measurements
of phase velocities, we investigated different dataset scenarios generated from different
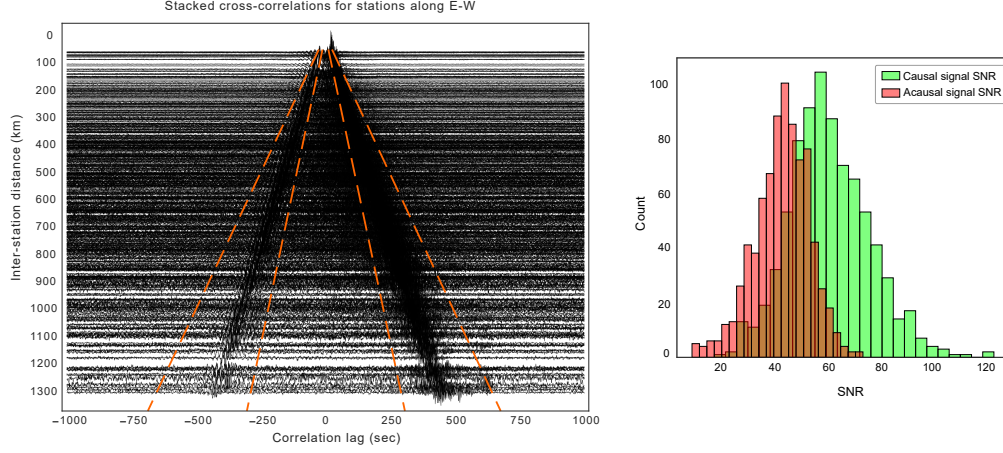time period of stacking. By comparing the results from a selected semi-homogeneous dataset

Figure 2. (Left) calculated EGFs for a subset of E-W paths between stations. Causal (positive lag) signals: east to west propagation, acausal (negative lag) signals: west to east propagation. The moveout lines (orange dashed lines) are drawn for 2 km/s and 4.5 km/s velocities. (Right) distribution of signal-to-noise ratios (SNR) for causal/acausal signals related to all EGFs from E-W paths measured in this study.

to the ones from our final inversions, we conclude that our final phase velocity measurements are reliable regardless of the observable non-uniform noise distribution in the data (see supporting information for discussion).

2.2 Dispersion Measurements

We calculated the inter-station Rayleigh wave phase velocity dispersion curves from the inter-station EGFs using the *GSpecDisp* program (Sadeghisorkhani et al., 2018). This is a MATLAB-based GUI software that is primarily designed to facilitate phase velocity dispersion measurements from stacked noise correlation functions in the spectral domain. There are two main modules included in this program that are developed for calculating a regional average dispersion curve (method of Prieto et al. (2009)), as well as individual inter-station dispersion curve measurements (method of Ekström et al. (2009)). Although an automatic selection process is available in this program, we manually selected the phase velocity measurements for all the EGFs.

314   For measuring phase velocities from the input stacked correlation functions at each

315 period, the real part of the input EGF spectrum is matched with the zero crossings of

316 appropriate Bessel functions. Phase velocity is obtained using the formula

$$C(\omega_n) = \frac{\omega_n}{Z_n + 2m}$$

317   where Z_n denotes the n-th zero crossing of the Bessel function, ω_n is the angular

318 frequency of the n-th zero-crossing of the correlation spectrum, and $m = 0, \pm1, \pm2, ...$

319 takes the 2π ambiguity of phase velocity (cycle skipping) into account. Due to the val-

320 ues of m, many possible dispersion curves can be measured for an EGF. Using the av-

321 erage dispersion curve measurement module of *GSpecDisp*, we first calculated a few dif-

322 ferent average dispersion curves by dividing the study area into sub-regions, based on

323 geology and tectonics. Next, we used those average curves as references to manually se-

324 lect the appropriate phase velocities for individual inter-station paths. A few represen-

325 tative examples of the individual dispersion measurements, as well as the regional av-

326 erage dispersion curve for the study area, are illustrated in Figure 3. As shown in this

327 figure, reliable phase velocity measurements at the longest periods (e.g., > 40 s) can only

328 be achieved from EGFs with longer inter-station distances (e.g., E55A-I64A and VLDQ-

329 I64A in Figure 3).

330   **2.3 Tomography Method**

331   There are direct and indirect approaches to extract shear velocity models from sur-

332 face waves. In the first approach, surface waves are directly inverted for a shear wave

333 velocity model (e.g., Debayle & Kennett, 2000; van der Lee & Frederiksen, 2005). Al-

334 ternatively, phase or group velocity maps at different periods are extracted as the first

335 step of the tomography procedure and then inverted for shear velocity information (e.g.,

336 Kao et al., 2013; Kuponiyi et al., 2017). In this study, we first recover Rayleigh wave phase

337 velocity variations at discrete periods from the calculated inter-station dispersion mea-

338 surements, and then we extract 1D dispersion curves from the generated phase veloc-

339 ity maps to be inverted for shear velocity profiles.

340   The tomography program requires the input inter-station phase velocities to also

341 include measurement errors. However, the *GSpecDisp* program does not give the mea-

342 surement errors. In this case, a fixed set of synthetic errors (reference errors) is assigned
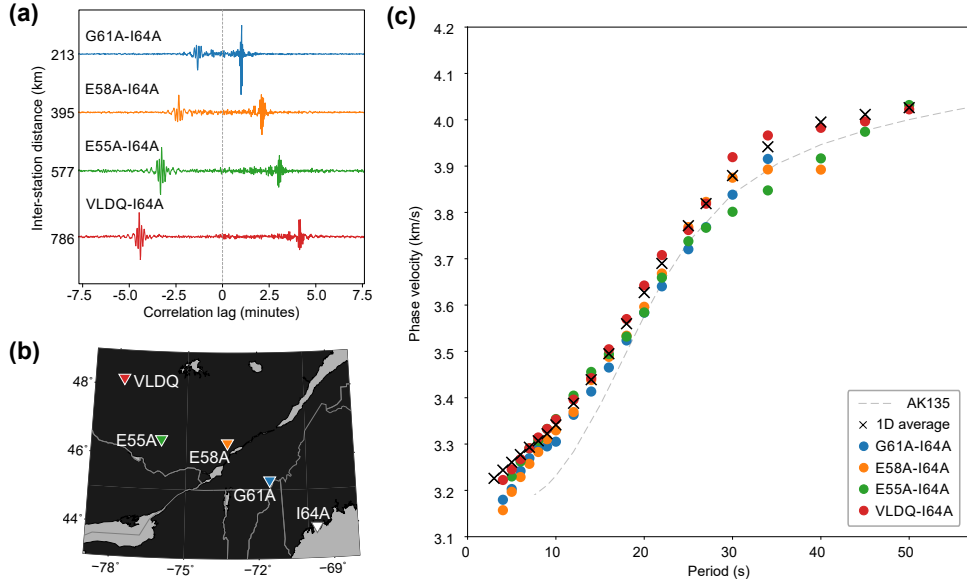
Figure 3. (a) Examples for EGFs related to station I64A cross-cutting various tectonic domains in the study area. (b) Map of the stations related to the shown EGFs. (c) Measured inter-station dispersion curves for the shown EGFs. The 1D average curve (cross symbols) represents the regional average based on all EGF measurements.

to the measurements, with errors typically increasing with increasing period. We argue that the measurement errors should be proportional to the EGF quality such that smaller phase velocity errors should be attributed to higher quality EGFs. Therefore, we calculated the SNR for the symmetrized EGFs and used the mean of these values as a reference to modify (increase/decrease) the measurement errors for each inter-station dispersion curve. Since the distribution of the calculated SNR values is very similar to a Gaussian distribution, we used the z-score (i.e., a real number that is the distance from the distribution mean given in terms of the number of standard deviations) of the SNR for each EGF and multiplied it by a small value of 0.002 to estimate the error adjustments from the reference errors for each period of the inter-station dispersion curves. This small value was decided experimentally after making sure that it does not cause the final measurement errors to be negative or too strongly deviated from the reference errors. The assigned measurement errors for periods in this study, 4-50 s, before and after the error adjustment process are 0.015-0.04 km/s and 0.0092-0.0438 km/s respectively.

We followed the tomography method described by Darbyshire & Lebedev (2009) to recover anisotropic phase velocity variations at periods from 4 to 50 s. This inversion method has been successfully implemented in previous studies using earthquake-based 2-station phase velocities (e.g., Deschamps et al., 2008; Petrescu et al., 2017; Foster et al., 2020), earthquake-to-station group velocities (e.g., Darbyshire et al., 2018), ambient-noise group velocities (e.g., Pawlak et al., 2012), and combined ambient-noise and earthquake 2-station phase velocities (e.g., McLellan et al., 2018). The inversion is performed across a triangular grid of nodes that are evenly spaced throughout the region covered by the surface wave raypaths. We set the model and interpolation grid spacing to 80 km and 20 km respectively.

Assuming a weakly anisotropic medium, the inversion solves for 5 unknowns in phase velocity at each node:

$$\delta C(\omega) = \delta C_{iso}(\omega) + A_1 cos(2\psi) + B_1 sin(2\psi) + A_2 cos(4\psi) + B_2 sin(4\psi)$$

where δC_{iso} is the isotropic phase velocity anomaly, and 2ψ and 4ψ are the anisotropic components for the phase velocity variations with π and $\pi/2$ periodicity respectively (Smith & Dahlen, 1973). The solutions are found by solving a system of linear equations governing relations between the average phase velocity along the paths, the horizontal sen-

sitivity area at the grid nodes (assuming zero-width rays), and phase velocity perturbations over the model grid. The model is regularized by adding smoothing and damping terms into the inversion kernel matrix that penalize the first and second derivatives of the recovered anomaly distribution. The damping applied by penalizing the second derivative of the variations for the neighboring nodes diminishes the patterns of anisotropy more strongly. Therefore, applying much larger smoothing parameters compared to the damping parameters is required (Figure 4; Foster et al., 2020). We tested many different regularization parameter values for isotropic and anisotropic components and chose an appropriate setting based on the regularization trade-off curves between the variance reduction and model roughness, as well as visual assessment of the resulting phase velocity maps. The isotropic and anisotropic regularization curves show the expected shape of trade-off curves, making it possible to select best approximate values from the curve knees (Figure 4; Figure S5-S6, supporting information). Since the resolution of the anisotropic components is generally lower, they were more strongly damped and smoothed (e.g., Darbyshire & Lebedev, 2009). We applied the same regularization parameters in the inversions to the phase velocity datasets at all periods for consistency (Table S2, supporting information).

Depending on the background noise level at the seismograph sites, the inter-station distance, and the number of stacked noise cross-correlation functions used in the generation of the EGFs, the frequency content of the dispersion measurements varies for different paths. This results in a notable difference in the path coverage at different periods. The number of crossing raypaths varies from a minimum of 183 (50 s period) to a maximum of 1429 (6 s period) with an average of 1106 rays (Figure S1, supporting information).

The dispersion datasets that were input to the tomography program must satisfy the following two criteria:

(i) The time domain signal to noise ratio (SNR) must be higher than 8.8 dB for the symmetrized EGFs (Figure S4, supporting information). This value is calculated using the $\mu-2\sigma$ formula for the SNR distribution of all possible EGFs, where μ is the mean SNR for the distribution, and σ is the standard deviation of the calculated SNR values. We use the formula $SNR(dB) = 20log(\frac{RMS_{signal}}{RMS_{noise}})$ to calculate SNR values, where RMS is the root mean square of signal or noise for window sizes calculated using 2 km/s and
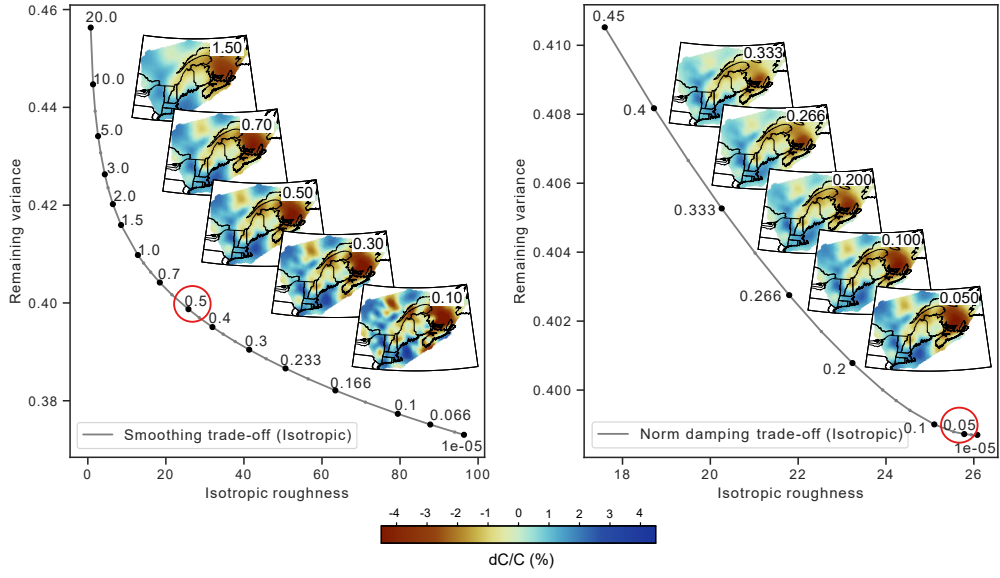
Figure 4. Inversion regularization trade-off curves for 16 s period. (Left) smoothing trade-off curve. (Right) damping trade-off curve. The red circles mark the values used in the final inversions. The maps illustrate the inversion results for the regularization parameter values marked at the top right corner of the maps. Only curves for the isotropic component are shown here; see Figures S5-S6 in supporting information for the other components.

4.5 km/s moveout velocities (Figure 2). By following this procedure, we exclude possible unreliable dispersion measurements from the tomography input datasets.

(ii) The associated wavelength (λ) of the input dispersion measurements must be shorter than one-third of the inter-station distance (Δ) for the average phase velocities (Figure S4, supporting information). Previous studies have mentioned unreliable measurements for $\Delta < 3\lambda$ (e.g., Bensen et al., 2007; Köhler et al., 2011).

In addition to the above two criteria, the inversion procedure also includes an outlier exclusion step in which spurious paths are found based on the inversion misfit, and subsequently excluded from the final inversions. After following the above procedure, we achieve a good azimuthal coverage for the input data used in the tomography. Due to the aperture of the study area, east-west directions (60°-120°) are the most common; however the full range of azimuths is covered and the selection criteria reduce bias (Figure S4, supporting information).

2.4 Shear Wave Velocity Inversion

In order to obtain shear velocity structure, we extracted local (1D) dispersion curves from 212 phase velocity map grid nodes, and inverted them for shear wave velocity profiles. Bathymetry information for all nodes was extracted from a global model (Amante & Eakins, 2009), and we fixed the water depth as the first layer in the inversion parameter file for the nodes located in water areas. The shear wave velocity models are then parameterized as one crustal layer and one mantle layer with 4 B-splines and 5 B-splines to describe velocity variations in the crust and mantle respectively. Crustal thickness solution in the inversions is an unknown parameter that was allowed to vary from 20 km to 60 km. We set the maximum depth of inversions to 200 km that fully covers the sensitivity of even the longest period of the phase velocities in this study (i.e., 50 s; Figure 5). We used the inversion approach of Guo et al. (2016), a Bayesian inference method that outputs a joint probability density function (PDF) in the model and data space that contains the ensemble of accepted models, for which the synthetic dispersion curve matches the data within errors. The posterior PDF is generated by data and updated prior information during the inversion process (Tarantola, 2005; Afonso et al., 2013). In this inverse problem scheme, due to parameter space being extremely large, a Markov Chain Monte Carlo (MCMC) sampling algorithm is adopted to sample the posterior distribu-
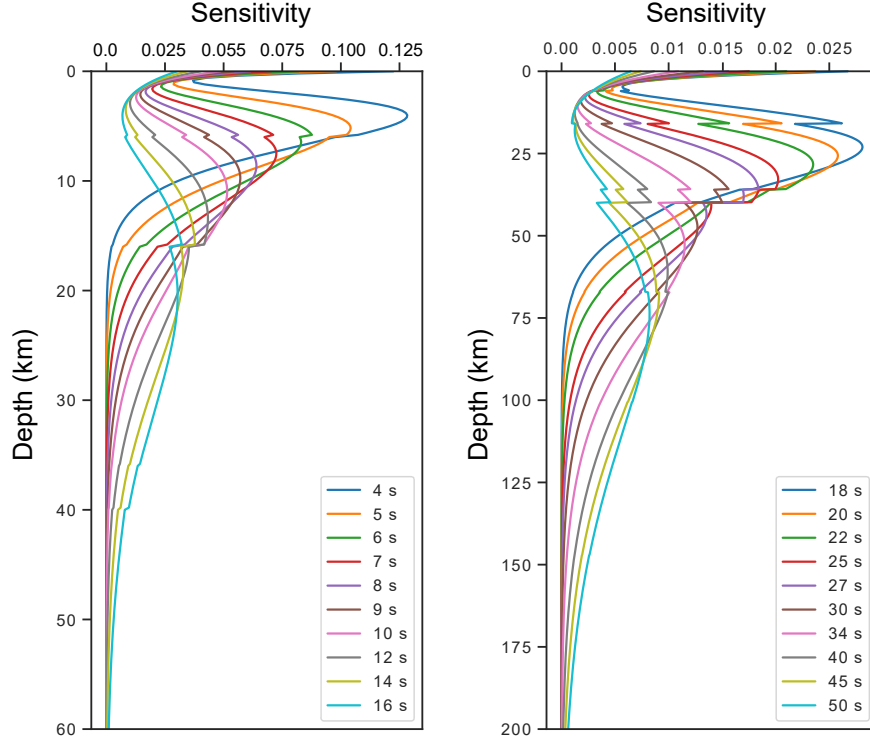
Figure 5. Fundamental mode Rayleigh wave depth sensitivity kernels for 20 periods used in this study. Note the difference between the axis ranges for these two subplots.

tion (Guo et al., 2016). As an example of the process, the regional average shear velocity profile resulting from the inversion of 1D average dispersion curve is shown in Figure 6.

We construct our (pseudo) 3D shear wave velocity model by extracting and combining the mean profiles from the posterior PDF results. Although the model is parameterized to 200 km depth, we present our shear wave velocity model down to 60 km depth for which the shear velocity variations are best resolved. We interpolated the shear velocity data at each depth using a finer grid spacing of 0.15°×0.10° while applying a Gaussian smoothing function with the smoothing length of 50 km to remove lateral variations that are unrealistically small. The cross-section data are extracted from the interpolated shear velocity models at each depth by sampling the shear velocity model at every 5 km distance along the tracks.
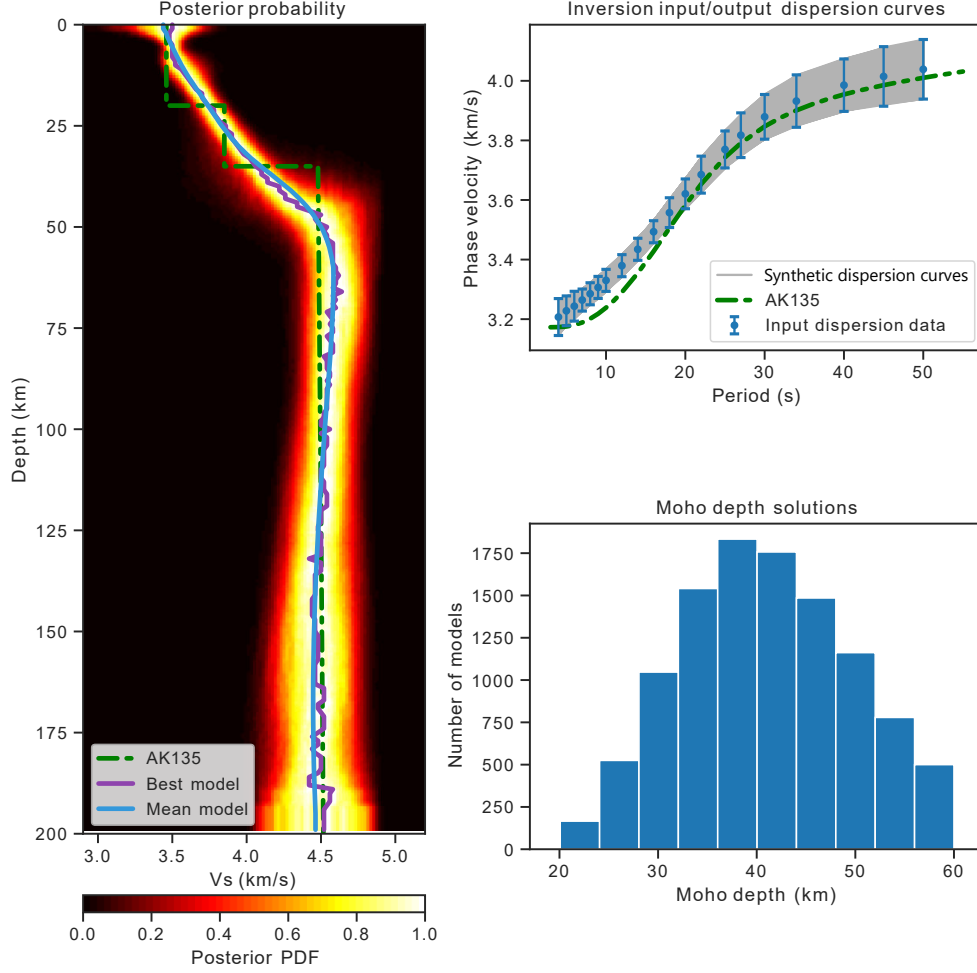
Figure 6. Shear velocity inversion results for the 1D average dispersion curve measured in this study. The left subplot illustrates the posterior probability density function (PDF) for this inversion. The top right subplot shows the input dispersion curves, as well as the forward modelled dispersion curves for the accepted solutions. The bottom right subplot is the histogram for the accepted recovered Moho solutions. The shear wave and dispersion profile of the global reference model AK135 (Kennett et al., 1995) are drawn for comparison purpose (green dashed lines).

To estimate Moho depths from the shear velocity models, we followed the method suggested by Kao et al. (2013). Accordingly, we calculated the typical crustal velocities (15-25 km depths), and typical mantle velocities (55-65 km depths) for each 1D shear velocity profile, and tested different percentage of increase from the typical crustal velocities toward the typical mantle velocities (Figure S17, supporting information). We finally chose the average between the estimates from 50% and 85% as the Moho depth proxy for each inversion node. Combining the resulting estimates at all inversion nodes, our final Moho depth map is generated.

3 Model resolution

We conducted various types of resolution tests at all periods and results for a subset of periods are presented in this paper. The selection of representative periods was made to cover a wide range of depths and a variety of path coverage levels (Figure 5; Figures S1-S2, supporting information). We chose 4 periods: 6 s (best path coverage; sensitive to upper crustal depths), 14 s (average path coverage; sensitive to mid-crustal depths), 25 s (average path coverage; sensitive to lower crust and around Moho depths), and 40 s (low path coverage; sensitive to sub-Moho depths). All resolution tests were carried out following the same framework: generating a synthetic input phase velocity model, adding 0.02 km/s random noise, and inverting the measurements for an anisotropic phase velocity solution with the same path coverage and inversion parameters as that applied to the real data.

In this section, we explain the resolution test results for some spike tests (equivalent to the conventional checkerboard resolution tests in tomographic studies) that were designed based on custom geometric shapes and also a synthetic model based on the observed anomalous patterns in the final phase velocity maps (Figure 7). Results for more resolution test types including more spike tests (stripe patterns; Figure S7), linear gradients (Figure S8), isotropic-anisotropic leakage tests (Figures S9-S10), and rotated anisotropy tests (Figure S11) are also available in the supporting information.

- Large hexagons with 320 km diameter (Figure 7, model A): Anomalies at all four representative periods are clearly recovered. The geometry of the hexagon centred at 72.5°W, 44°N is perfectly reproduced with almost no smearing effect. The other hexagons that are closer to the edges of the phase velocity maps show a min-

imal smearing effect at the hexagon edges that are the closest to the margins of the study area, which is expected given the density of crossing rays in those areas. In terms of amplitude recovery, anomalies are very well reproduced with better recovery for the two hexagons centred at 72.5°W, 44°N (New Hampshire), and 65°W, 45°N (Nova Scotia - New Brunswick), even at the longest periods (i.e., 40 s), compared to the others. Weak spurious anisotropy is observed in the margins of the study area, especially evident in the north and south in the 40 s map.

- Small hexagons with 160 km diameter (Figure 7, model B): These small hexagon patterns have an edge size of 80 km, and are separated by ∼160 km distance. The two anomalies located in the northeast of the study area near the Newfoundland coast are not recovered. The four anomalies in the centre of the study area and the one over Nova Scotia are very well reproduced in terms of their amplitude and geometry. Other hexagons situated near the southern, western, and northern edges of the maps are adequately recovered, but with some smearing effects observable due to an insufficient path coverage in these areas. Comparing the anomalies in the northern edge of the study area with those situated along the eastern edge of the maps, the amplitude recovery of the hexagons in the eastern edge is better. In general, smearing at the edge areas is present and this effect is similar along different edges of the maps. Spurious anisotropy is minimal in the centre, but this effect is observable at the edge areas, especially in the north, in Nova Scotia, and the southeastern edge.

- Small triangles with 160 km edges (Figure 7, model C): These triangles are approximately the size of the average station spacing, and the smallest spike patterns that we tested in this study. The triangles are separated by ∼240 km on average. Despite being very small features, the majority of the anomalies located in Nova Scotia, northern New Brunswick, NE USA (SE Maine, Massachusetts - New Hampshire), southern Quebec, and eastern Ontario are very well recovered. Similar to the "small hexagons" tests, anomalies in the far northeast of the maps are not recovered. The magnitude of the anomaly in the north, centred at 71°W, 49.5°N, is greatly reduced at all periods; nonetheless, this anomaly is still detectable. In this test, small spurious anisotropy is observable in Nova Scotia and at the NW edge of the study area.

- Based on the observed slow anomaly patterns in the final phase velocity maps, we created a synthetic input model for our study region (Figure 7, model D). The anomalies in this test are recovered very well throughout the maps at different periods. Even in the northeast of the Gulf of St. Lawrence, and in the north where other tests fail or have difficulty recovering the synthetic input anomalies, this test suggests that the main observed patterns in the final phase velocity maps are robust model features. Amplitude recovery gets less robust at longer periods; however, all anomalies stay detectable at all periods. Anomaly smearing is minimal overall, but this effect is still observable in the northeast and the north of the maps. Spurious anisotropy in the north and northeast of the study area is also observable in this test.

- Other resolution tests are also available in the supporting information (Figures S7-S11). We provide a very brief summary of those results here and readers are referred to the supporting information document for a more detailed discussion. The stripe pattern resolution tests are available in two directions: stripes along NE-SW (models S1-S2), as well as stripes with NW-SE direction (models S3-S4). These tests are presented for two different width configurations (240 km and 80 km), and our analysis suggests that they are all very well recovered (Figure S7). The next set of tests are the linear gradient patterns that are conducted for two different directions (models G1 and G2; Figure S8). These tests are useful to investigate the bias due to a dominant number of paths along a specific direction. The linear gradient model G1 (i.e., along NW-SE direction) is better recovered than the model G2 (i.e., along NE-SW direction), especially at the longest periods (25-40 s). Due to the trade-off between isotropic and anisotropic structure, leakage between the isotropic and anisotropic components exists in the inversion of surface wave velocity. This may result in a non-robust feature looking robust (or vice versa), and therefore overinterpreting the results. Hence we tested this effect by only inputing one component of the model as the synthetic model (isotropic or 2ψ or 4ψ), and recovering the models to investigate the leakage effect. The results for this test suggest a very small leakage between the surface wave components. Finally, to investigate the robustness of our anisotropy models, we rotated the 2ψ anisotropy results by 90° and used them as input synthetic models at each
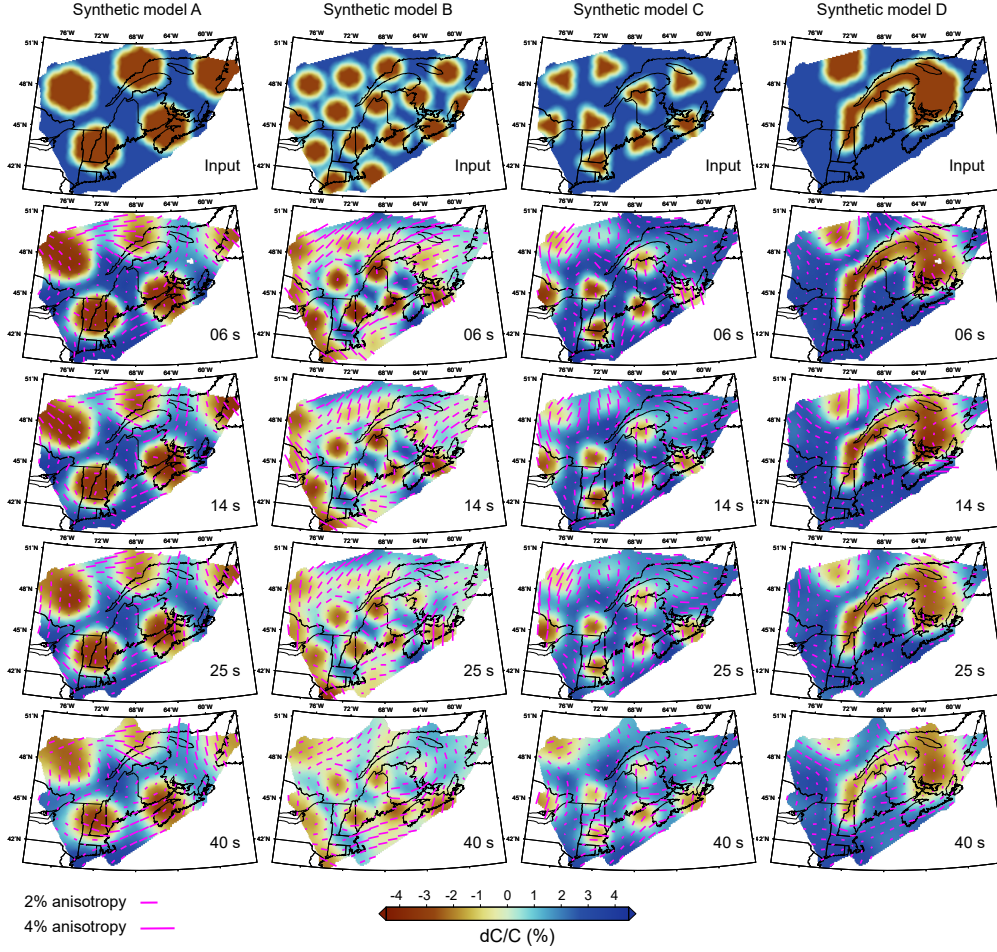
Figure 7. Structural resolution tests (spike tests) for the 4 representative periods (marked at the bottom right of each map). Results are shown for: A - large hexagons (320 km diameter), B - small hexagons (160 km diameter), C - small triangles (160 km edges), D - structure based on tomography results.

period to be inverted and checked for the recovery level. The results of this test also suggests that our anisotropy results are reliable overall.

4 Results

4.1 Phase velocity model

The final phase velocity maps and maps of ray coverage at a selection of periods from 5 s to 40 s are shown in Figure 8. Full sets of phase velocity maps and raypaths are available in supporting information (Figures S12-S13). As discussed in Section 2.3,
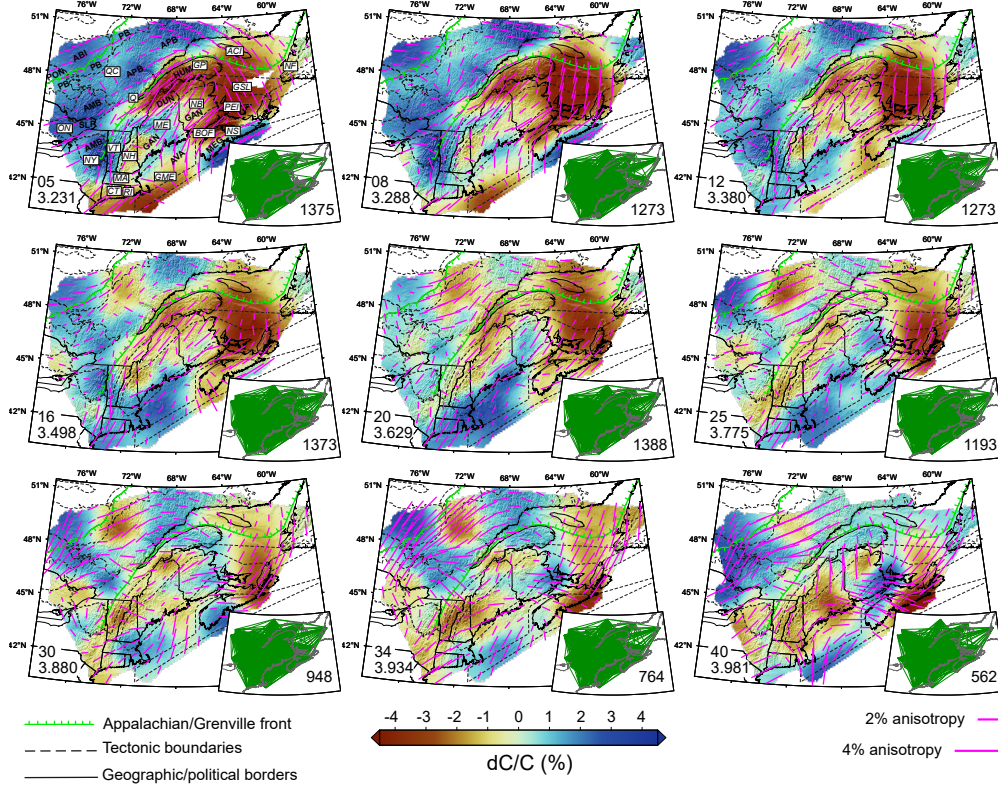
Figure 8. Final phase velocity maps and corresponding raypath coverage (small maps at the bottom right corner of the phase velocity maps; the number at bottom right is the number of rays) for a subset of periods in this study. The magenta bars represent the 2ψ anisotropy variations. The two numbers at the bottom left corner of the maps denote the period (s) and average phase velocity (km/s) respectively. Acronyms are explained in Figure 1.

we invert the inter-station dispersion datasets for isotropic, 2ψ, and 4ψ components. However, we only interpret the maps of isotropic and 2ψ components, as the 4ψ component is not well constrained by the data and it is typically small.

Rayleigh wave phase velocity variations at each period give integrated shear velocity information over a depth range explained by depth sensitivity kernels (Figure 5). We use these kernels to understand the sensitivity of the phase velocity maps to the subsurface structure at different depths.

At short periods, 4-12 s, Rayleigh waves are predominantly sensitive to upper crustal depths ($<\sim$15 km). We observe $\pm$5% perturbations of phase velocities relative to the regional average at these periods. In contrast to the eastern Grenville and the SE Su-

perior, the northern Appalachians are dominated by generally slower than average phase velocities. Slow anomalies are observed across the Gulf of St. Lawrence (GSL), Bay of Fundy (BOF), Gaspé Peninsula, along the St. Lawrence River, and beneath the Gulf of Maine (GME). In the easternmost study area, a slightly faster upper crust in Meguma than Avalonia is recovered. Almost the whole of Ganderia is dominated by slower than regional average phase velocities, except for a small fast anomaly that is observable close to the coastline in the west of BOF. Phase velocities of the Humber margin and the Dunnage zone are generally very similar in the northern Appalachians. While phase velocities in the SE Superior suggest a simple faster than average upper crust, more complex variations are observed in the Grenville Province. A relatively small and weak slow anomaly in the northwest of the study area (periods > 10 s), and also a small region to the west of the Appalachian front along the St. Lawrence river are observed.

At intermediate periods, 14-20 s, the maximum sensitivities are to mid-crustal depths from ~15 to ~25 km (Figure 5). The observed anomalies in the phase velocity maps at these periods are generally weaker than those observed at periods sensitive to upper and lower crustal depths (~ ±3%). The slow anomaly in GSL is less strong at the intermediate periods compared to the short periods. We observe a fast structure (~2% anomaly) beneath GME, and this feature extends to the northeast crosscutting the three easternmost domains (Meguma, Avalonia, Ganderia) at longer periods (18-20 s). The Humber and Dunnage zones are dominated by slow anomalies, and the Grenville and Superior are generally faster than the Appalachian domains. In the Grenville, we observe a prominent localized slow anomaly (~2%) situated in the northwest of the study area. A localized faster zone is also observed beneath the AMB zones in the Grenville Province.

At longer periods, 22-34 s, phase velocities have their maximum sensitivities to lower crust and around the Moho depths (25-45 km). At these periods, we observe ~ ±4% phase velocity perturbations from the regional average. The NE-trending fast anomaly crosscutting the three easternmost tectonic domains is a striking feature. A slow anomaly located in BOF extends into the central part of this NE-trending anomaly at 30-34 s periods. The Dunnage zone and Humber margin are dominated by prominent slow anomalies (~1-2%). A strong slow anomaly of 3-4% is observed beneath GSL. Fast anomalies in the Appalachians are observed beneath New Brunswick and southern PEI (27-34 s), and also under Gaspé peninsula (30-34 s). In the Grenville, the SLP zone is dominated by slow velocities at 22-34 s. The AMB zone at these periods is also faster than the other

regions in this orogen. The slow anomaly in the northwest of the study area is still a prominent feature, whereas the Superior province is ∼2% faster than the regional average.

The longest periods in this study (>34 s) are mostly sensitive to the depths around the Moho and uppermost mantle (45-60 km). With respect to the regional average velocities, we observe ∼ ±4% variations across the study area at these periods. Fast anomalies (2-3%) in the Appalachians are observed beneath the GME and southern Maine, under New Brunswick, SW GSL and southern PEI, and southern Nova Scotia (∼3%). Most of the Humber and Dunnage zones are dominated by slow anomalies with 1-2% strength at the longest periods, except for a ∼1% fast anomaly observed in Gaspé peninsula at 34-40 seconds, as well as a fast anomaly observed south of Quebec City at 50 s. In the Grenville orogen, the slow anomaly in the northwest gets weaker at periods longer than 34 s and it is eventually replaced by a 1-2% fast anomaly at 45 s. While the AMB zone in the north (76°W, 46.5°N) is recovered as a fast anomaly, the AMB zone in the south (in New York) is dominated by 1-2% slower than average velocites at 40-50 s. The Superior craton is recovered as a relatively fast (∼2%) anomaly at the longest periods (e.g., 40 s).

In terms of 2ψ anisotropy variations, weak to moderate anisotropy of ∼1-3% is observed across the study area at different periods. Overall, a ∼0.5-1% stronger anisotropy is observed in the Appalachians than the Grenville province. The predominant directions of the recovered anisotropy variations are typically along the general tectonic trend (i.e., NE-SW). Across GSL and the NE part of the study area, where the path coverage is limited, the direction of anisotropy is almost perpendicular to the tectonic trend (N-S and NW-SE) at the shortest (4-12 s) and longest periods (> 30 s). However, at the intermediate and long periods (14-30 s) where these areas are best covered by the datasets, the anisotropy trend beneath this region follows the general tectonic trend. The slow anomaly in the northwest of the study area that is visible at 10-40 s period shows a different characteristic to surrounding areas, with a slightly stronger anisotropy, as well as up to 30° difference of anisotropy directions. We also notice a change in the direction of anisotropy when comparing the results for the Appalachian and the Grenville domains on either side of the Appalachian structural front, especially near the SLP. Across eastern New Brunswick where a strong fast anomaly is observable at the longest periods (> 30 s), the anisotropy variations are recovered as E-W to SE-NW orientations.

4.2 Shear velocity model

As discussed in Section 2.4, we construct our 3D shear velocity model from the inversion results of the extracted 1D dispersion curves. The maps of shear velocity variations at different depths are presented in Figure 9 (see also Figures S14-S16, supporting information). To gain more perspective from the shear velocity model, we have also made cross-sections crosscutting different tectonic domains in the study area (Figure 10).

At upper crustal depths (< 15 km), our shear velocity model shows a considerable range of variations from 3.2 km/s to 3.75 km/s. The observed pattern of variations in the shear velocity model at these depths follows the geographical distribution of the units including various tectonic terranes and sedimentary basins. Similar to the observations of phase velocities, we notice that the SE Superior and the eastern Grenville Province have generally faster upper crustal structure than the northern Appalachians. In the Appalachians, localized fast velocity anomalies are observed in ∼10-15 km depth maps under southern Nova Scotia (Meguma), across GME (Avalonia), and southwestern part of the Humber and Dunnage zones. The strongest slow anomalies (< 3.4 km/s) are recovered at the shallowest depths (< 10 km) beneath the GSL extending into BOF, under GP and NE St. Lawrence River, and in the far south of the study area beneath the GME. The thickness of these slow anomalies varies from 8-10 km beneath the GSL, to 5-6 km beneath the GP and NE St. Lawrence River, and ∼3-4 km under the BOF and in the extreme south of the study area in the GME. A similarly strong slow anomaly is also recovered at depths < ∼3 km beneath the SLP in the Grenville Province (Figure 10-DD'; Figure S14, supporting information). In general, the velocity structure of the upper crust beneath the eastern Grenville and the SE Superior does not appear to be as complex as the northern Appalachians, but our model suggests a clearly heterogenous strucure beneath these regions. Faster regions at this depth range are observed beneath the SE Superior Province, the southern AMB domain (in New York), and in the north of the study area. A relatively slow anomaly is observed at depths > 12 km in the northwest of the study area. We also observe a velocity contrast across the Appalachian front, with higher velocities observable in the Grenville side at upper crustal depths (e.g., 13 km, Figure S14, supporting information). A similar velocity contrast occurs further to the southeast into the Appalachians at deeper intermediate crustal depths. Our shear velocity model does not distinguish the Grenville Province from the Superior craton at depths < 10 km,
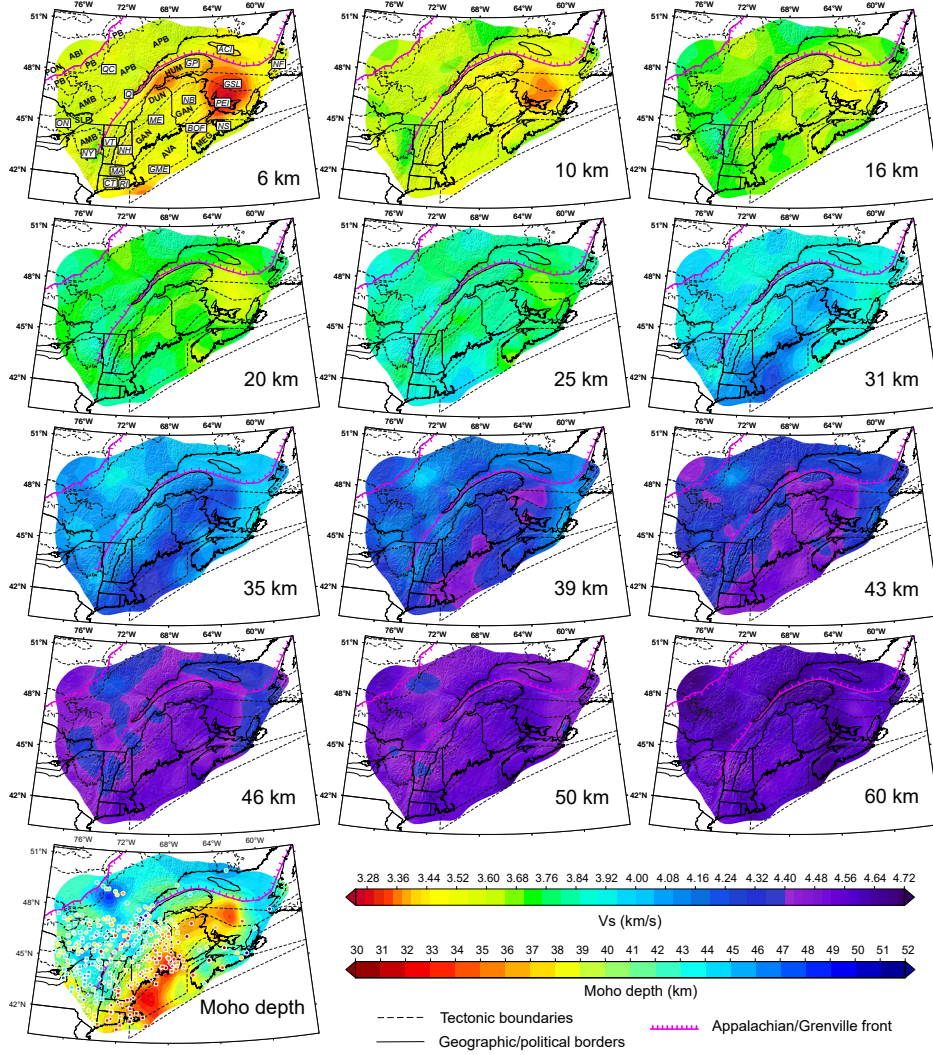
Figure 9. Final shear wave velocity maps at different depths. The map at the bottom left illustrates our Moho depth using the average of 50% and 85% velocity increase proxies (see text for more information). The scatter points on this map are the Moho estimates from previous studies (only a subset of their results are shown here; circles: Darbyshire et al. (2017, and references therein), diamonds: Li et al. (2018), squares: Shen & Ritzwoller (2016)). See supporting information document for extra Moho depth maps estimated using different proxies (Figure S17) and also additional shear velocity maps (Figures S14-S16). Acronyms are explained in Figure 1.
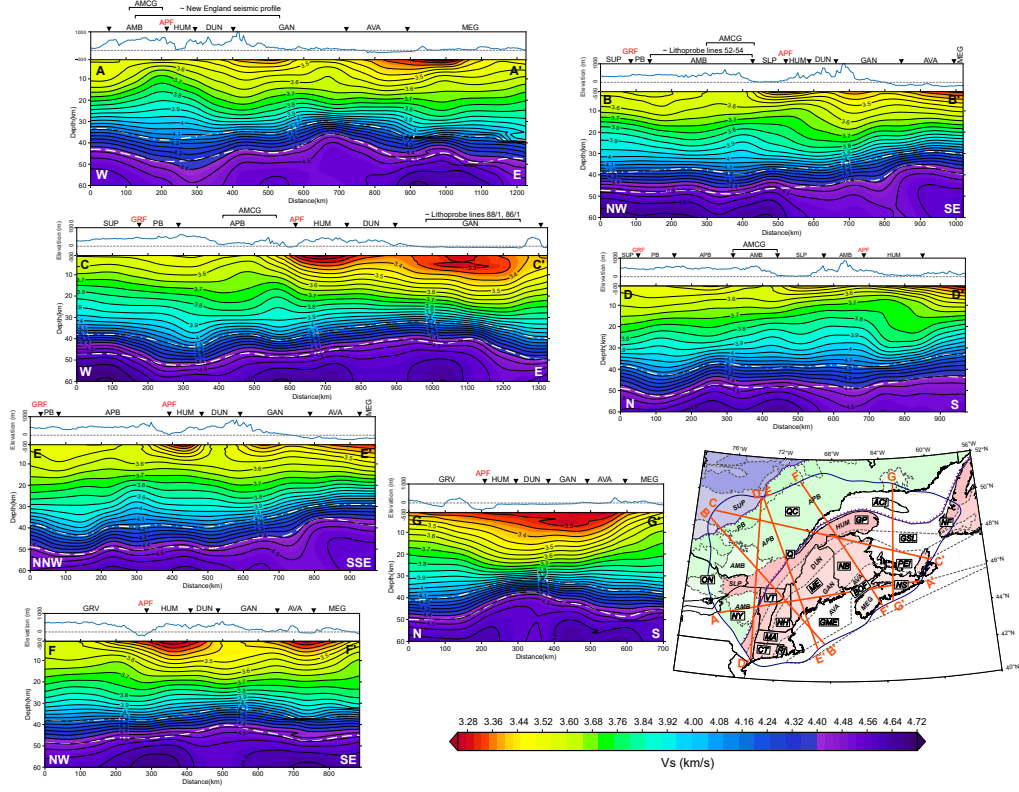
Figure 10. Cross-sections from the final 3D shear wave velocity model along five different profiles. The map at the bottom right denotes the location of the profile tracks. Our inferred Moho depths using the average of 50% and 85% velocity increase proxies are shown by the dashed white lines in the illustrations. Land elevation / water depth for each profile is shown above the velocity models. SUP: Superior, AMCG: anorthosite–mangerite–charnockite–granite, other acronyms are explained in Figure 1. Vertical axis of the velocity profiles is 6 times exaggerated.

but a systematically faster Superior is recovered at the deeper depths covered by this study.

At intermediate crustal depths (15-25 km), shear velocities in our study area vary between ∼3.5 and 4.0 km/s suggesting significant variations in relative thickness of upper crust to lower crust (Figures 9, 10). At these depths, fast regions include GME, western SLP and the southern AMB zone, and the Superior Province. Slowest regions at these depths are recovered beneath the GSL, central Ganderia domain, and the far SE of Nova Scotia. Investigating the shear velocity model at depths from 25 to 45 km, we observe velocity variations in ∼3.75-4.50 km/s range. This relatively wide range of shear velocity variations include both typical crustal and mantle velocities suggesting that the crust-mantle boundary in many regions of our study is likely situated within these depths. The observable fast regions in the Appalachians follow a SW-NE trend covering GME, southern Maine, New Brunswick, and the southwestern GSL crosscutting the three Appalachian coastal domains. Parallel to this fast anomaly to the north, our shear wave velocities are 0.1-0.2 km/s lower indicating a strong velocity contrast occuring near the Ganderia-Dunnage boundary. Further northwest, crossing the Appalachian front, we observe a small increase of shear wave velocities at depths >∼30 km in the Grenville side. Maps of shear wave velocities at lower crust to Moho depths (25-45 km) are indicative of heterogenous eastern Grenville seismic structure. A striking slow anomaly in the NW of the study area is observed with velocities < 4.4 km/s at 35-50 km depths. We also observe a weaker slow anomaly centered beneath the western SLP and expanding toward the AMB zones in the Grenville Province at these depths. Investigating the shear velocity maps at mantle depths (> 50 km), a general increase of shear velocity with age is suggested for the first order tectonic domains (Superior > Grenville > Appalachians). However, the uppermost mantle structure beneath southern New Brunswick and southwestern Nova Scotia is considerably (∼0.2 km/s) faster than other tectonic domains of the Appalachians.

The cross-section illustrations provide evidence for a very complex 3D crustal velocity structure beneath the study area (Figure 10). The prominent shallow low-velocity zones (<3.4 km/s) beneath the southern GSL (profiles CC', GG'), Bay of Fundy (profiles AA', FF'), Gulf of Maine (profiles BB', EE'), St. Lawrence river (profiles CC', EE', FF'), and St. Lawrence Platform (profiles BB', DD') have very different thicknesses from less than 3 km to a maximum of 10 km. Near the major surface tectonic boundaries (i.e., Appalachian/Grenville fronts), our cross-section illustrations suggest significant lateral

690 heterogeneities at all depths covered by this study. The Moho depth variations from the

691 two shown proxies across different tectonic domains indicate that the crustal thickness

692 can be highly variable over a short distance (e.g., profiles EE', GG'; ∼10 km variations

693 over ∼100 km distance).

5 Discussion

695 Although ambient noise tomogaphy is inherently insensitive to fine stratigraphic

696 details, our models reveal unprecedented details of the crust and sub-Moho structure be-

697 neath the study area. This enables us to discuss the observed features in terms of their

698 tectonic implications. We note that due to the highly nonlinear relationship between the

699 lithology and seismic velocities (e.g., Fountain & Christensen, 1989), we have been care-

700 ful to not interpret the results in terms of variations in lithology. That said, our reso-

701 lution analyses suggest that the variations of seismic velocities at the scale of tectonic

702 zones and subprovinces are well constrained.

5.1 Thickness of the sedimentary layers

704 According to depth sensitivity kernels and the shortest periods covered by this study

705 (Figure 5), we should be able to resolve the geometry of the sedimentary layers with thick-

706 ness > ∼3 km. In our 3D model, shear velocities lower than ∼3.4 km/s are interpreted

707 as sedimentary layers. Accordingly, the thickest sedimentary layer in our study area is

708 located beneath the GSL and PEI (Figures 9, 10) with a thickness of ∼8-10 km. This

709 sedimentary basin has a U-shaped geometry with the maximum thickness located be-

710 neath PEI. Our interpretations are consistent with the previous ambient noise tomog-

711 raphy study carried out over the GSL (Kuponiyi et al., 2017). The next thickest sedi-

712 mentary layer is located under the NE St. Lawrence River and beneath the Humber mar-

713 gin with a thickness of ∼5-6 km. This sedimentary layer was developed after break-up

714 of Rodinia at ∼615 Ma which resulted in producing extensional features including failed

715 rift arms of the St. Lawrence (e.g., S. Kamo et al., 1995; S. L. Kamo et al., 1989). Across

716 the BOF, thickness of the sedimentary layer is likely to be ∼3-4 km. Although our shear

717 velocities are not best constrained at depths < 3 km, we note that the thickness of the

718 sedimentary layer may be ∼1-2 km beneath the eastern SLP.

5.2 Crust-Mantle boundary

Variations in our Moho depth map agree well with the results from previous studies that used receiver function techniques and joint inversion of surface waves and receiver functions (Figure 9). Due to the nature of the depth sensitivity kernels (Figure 5), surface wave techniques are relatively insensitive to sharp discontinuities, resulting in models with a transitional crust-mantle boundary. However, as discussed by previous authors (e.g., Kao et al., 2013), implementing proxies defined as a certain increase from typical crustal velocities to typical mantle velocities enables us to have acceptable estimates for Moho depths, as well as relative variations of Moho thickness across the study area (Figure S17, supporting information).

The Grenville Province and the northern Appalachians have experienced different tectonic formation and evolution mechanisms, including their temperature regime, the spatial scale of the terranes involved in the orogenesis and the duration of accretion and collision. This difference is clearly manifested in our Moho depth estimates derived from the 3D shear velocity model. The crust beneath the Grenville orogen is typically thicker than the Appalachian province (except for Nova Scotia and southern New Brunswick). Average crustal thickness resolved by our Moho proxy of choice in the Grenville orogen is ~40-45 km, which is consistent with the estimates from previous seismic studies (Figure 9; Shen & Ritzwoller, 2016; Li et al., 2018; Darbyshire et al., 2017, and references therein). The deepest crust-mantle transition (> 50 km) occurs in the northwest of the study area, centred at 73°W, 49°N, in the Grenville Province (Figure 10, profile CC'). This localized feature is coincident with a negative Bouguer gravity anomaly in southeastern Canada (e.g., Ludden & Hynes, 2000). Interpretation of the Lithoprobe seismic profiles also suggests a thicker crust within the southern vicinity of the Grenville front (Martignole & Calvert, 1996). While our results suggest a thick crust beneath this region, results from previous receiver functions suggest a relatively shallower Moho (Figure 9). This anomalously thick crust is situated between the Allochthon Boundary Thrust (ABT, the boundary between PB and APB at the surface; Figure 10, profile EE'; e.g., Rivers, 2015) and Interior Magmatic Belt (IMB, located in central Grenville, marking the northern limit of post-Grenville magmatism; e.g., Hynes & Rivers, 2010). Thus the location of this feature suggests that it likely formed during or before the Grenvillian orogenic phases. A thicker crust than the average in the Grenville is also suggested beneath the younger SLP and the western AMB zones (45-50 km; Figure 9).

Crustal thickness variations across internal tectonic boundaries of the Appalachians do not seem to have clear systematic signatures. They rather suggest a very complex geometry manifested in significant heterogeneity within tectonic domains. While a generally shallower Moho is suggested beneath Ganderia compared to other tectonic domains of the Appalachians, the thinnest crust in our study area is observed beneath Gulf of Maine (Avalonia) and Gulf of St. Lawrence (Dunnage zone) (Figure 9; Figure 10, profile EE'). We suggest a ∼40-45 km crustal thickness beneath southern Nova Scotia, very similar to the suggested Moho depths beneath the Grenville orogen. A relatively large difference between our Moho proxies suggests that the Moho discontinuity beneath this area is likely to be a gradual interface (Figure 10, profile FF'; Figure S17, supporting information). In the same region, receiver function measurements suggest a significantly thinner crust (30-40 km; Darbyshire et al., 2017, and references therein). Although the results from a surface wave study cannot be directly compared to results from receiver functions due to the inherent differences in their methods, the mismatch between our inferred Moho depths and the results from previous receiver function studies for southern Nova Scotia suggests a complex crust-mantle transition beneath this region.

Some of our cross-sections are constructed along previously conducted active seismic profiles in our study area, and the results are generally in good agreement (Figure 10, profiles AA', BB', CC'). The New England seismic refraction/wide-angle reflection survey was conducted in the late 80s, and crosscuts four USA states from west to east: New York, Vermont, New Hampshire, and Maine (Hughes & Luetgert, 1991). It included both the Grenville and Appalachian Provinces and imaged a complex multi-layer crustal structure in the Appalachian terranes, an eastward dipping Grenvillian basement under the Appalachians, and a progressively shallower Moho beneath the Appalachian orogen. These findings are consistent with our observations in shear velocity profile AA'. The locations of Lithoprobe lines 52-54 coincide with a portion of shear velocity profile BB'. Noteworthy observations are a complex and laterally heterogenous seismic structure beneath this region with variable Moho depth geometry, and extension of Parautochthonous Archean basement to more than 200 km southeast of the Grenville front reaching the Moho (Ludden & Hynes, 2000). The Lithoprobe reflection-refraction lines 86/1-88/1 in southern GSL infer an increase in crustal thickness toward northeastern Nova Scotia (Hall et al., 1998), which is similar to the geometry suggested by our shear velocity model beneath this region (profile CC')

Previous receiver function studies have noted a sharp Moho offset occurring within a narrow zone in the central northern Appalachians, interpreted as the boundary separating the Laurentian (Grenvillian basement) and Gondwanan units at depth (Li et al., 2018, 2020). A supporting evidence for this interpretation is that this NE-SW trending Moho contrast feature is very well correlated with the trend of Peri-Gondwanan magmatic arc assemblages in Ganderia at the surface (e.g., Macdonald et al., 2014). Our maps of shear velocities and Moho estimates are consistent with this interpretation, and a step-like Moho geometry near the Ganderia-Dunnage boundary is suggested. The geometry of this feature in our model does not perfectly follow the surface tectonic boundaries, however. Instead, we suggest an oblique geometry (relative to the average NE-SW tectonic trend) for the eastern edge of the Grenvillian basement beneath the Appalachians. In the northeast, the eastern edge of the Grenvillian basement is likely located in the south of the Gaspé peninsula near the Humber-Dunnage surface boundary, whereas it occurs within Ganderia in the southwest. This observation supports the view that Laurentia may have experienced a variable orogenic (or post-orogenic) modification along its eastern edge in the northern Appalachians (Li et al., 2020).

5.3 Crustal anistropic fabrics

The past tectonic events in our study area may have overprinted older orogenic trends at different depths. Our period-dependent 2ψ anisotropy results can be interpreted in terms of deformations due to past tectonics. In particular, significant variations of anisotropy magnitude and/or direction with period, as well as variations over a short distance are investigated. We note that the resolution of our anisotropy results is much lower than the isotropic component. We therefore limit our interpretation of the anisotropy results to areas where a decent azimuthal coverage is provided by the inter-station dispersion datasets. For example, the anisotropy beneath the central part of our study area across the Appalachian front, southeastern Nova Scotia and beneath the Bay of Fundy are likely well-constrained, whereas limited azimuthal coverage over the GSL does not permit us to include this region in our interpretations (Figure S3, supporting information).

As discussed in Section 4.1, the dominant direction of anisotropy generally follows the geological trend. That said, interesting short scale variations of anisotropy are observable in different regions at different periods. For example, we observe localized variations of anisotropy, likely related to Mesozoic rifting, in Bay of Fundy manifested by

a change in the direction of anisotropy, from NE-SW to E-W and SE-NW orientations, at intermediate to longest periods of this study. Previous shear wave splitting results suggested a large splitting time ($\delta t > 1$ s) that requires a plate-scale anisotropic layer spanning both the crust and mantle beneath this area (Gilligan et al., 2016). While our model supports this interpretation, we note E-W anisotropy orientations with strong anisotropy beneath southern Nova Scotia and New Brunswick at periods sensitive to lower crust and lithospheric uppermost mantle depths. A westward (present-day coordinates) flat subduction of the Acadian lithosphere may have overprinted the crustal anisotropic fabric in the Middle Paleozoic (Bagherpur Mojaver et al., 2021).

We note a change in the dominant direction of anisotropy across the Appalachian front beneath the eastern AMB and SLP domains that is mainly evident at periods mostly sensitive to mid-to-lower crustal depths, between 7 and 27 s. While the direction of 2ψ anisotropy on the Appalachian side of this boundary is generally parallel to the main tectonic trend, the anisotropy directions in the SE Grenville orogen are almost perpendicular to this orientation. The maps of azimuthal coverage and our resolution analysis suggest that the 2ψ variations beneath this region are well constrained (Figures S3, S9-S11, supporting information). Results from previous shear wave splitting studies also suggest a similar E-W fast axes orientation near the Appalachian front (e.g., Darbyshire et al., 2015). Surface geology corresponds to the mafic Adirondack terrane containing anorthosite massifs dated between 1.1 and 1.3 Ga (Rivers et al., 1989). This age pre-dates the Grenville orogenesis suggesting that maybe the observed E-W direction of anistropy is a pre-Grenvillian fossil crustal fabric that has remained intact. Alternatively, it is also possible that thermal and melt weakening due to the rise of asthenosphere after delamination of the lithosphere beneath the orogenic lid caused lateral flow of the lower-mid crust modifying the crustal anisotropic fabric (the collapsed large hot orogen model; e.g., Rivers, 2015).

5.4 Tectonic implications

Variations in the relative thickness of the lower crust and upper crust carry information about crustal evolution due to past tectonic processes (e.g., Brown, 2010). Comparing the Grenville and Appalachian provinces, the lower crustal layer (shear velocities in ∼3.8-4.4 km/s range) beneath the Grenville orogen is generally thicker. This is especially evident in the western shear velocity sections (Figure 10, BB', CC', EE'). High velocity lower crust beneath the Grenville Province is consistent with protracted preser-

vation of a partially eclogitized root at the base of the crust (Darbyshire et al., 2017, and references therein). A relatively thick and fast lower crust in the central Grenville Province may also be marking the southeastern extent of the highly reflective Archean Parautochthon at lower crustal depths (Hynes & Rivers, 2010). This is compatible with the interpretation of Lithoprobe lines 52-54 that suggests the ABT reaches the Moho (Ludden & Hynes, 2000). Results from these reflection profiles suggest that the Superior craton continues as a wedge into the Grenville lower crust 200-300 km southeast of the Grenville front (Rivers, 1997; Ludden & Hynes, 2000).

The Grenville Province contains a significant amount of anorthosite with ages predating the Grenvillian orogenic phases (Musacchio et al., 1997; Hynes & Rivers, 2010). It is suggested that Grenville lower crust in the Mid-Proterozoic was significantly modified by the emplacement of these mafic intrusive units (Musacchio et al., 1997). The signature of these events is also manifested in the present-day seismic structure of the Grenville crust by high Vp/Vs ratios (e.g., Levin et al., 2017), and high shear velocity lower crust (e.g., Petrescu et al., 2016). Our shear velocity model suggests that the anorthosite–mangerite–charnockite–granite (AMCG; Figure 10) complexes including anorthosites in the Adirondack mountains (Marcy Anorthosite; profile AA'; Musacchio et al., 1997), anorthosites in the Morin terrane (Morin Anorthosite; profiles BB', DD'; Martignole & Calvert, 1996), and the AMCG unit in the central APB domain (Lac St-Jean AMCG; profile CC'; Hynes & Rivers, 2010), all have higher seismic velocities than their surrounding terranes at upper crustal depths. Investigating our shear velocity cross-sections, it is also evident that these AMCG units are underlain by localized high shear velocities at lower crustal depths, as well as relatively thicker crust (Figure 10). However, the high velocity lower crust and deeper Moho signature of these features are not exactly beneath the surface AMCG units, and they are shifted toward the Appalachian front (e.g., profile CC', Figure 10). This may provide evidence for ductility of middle and lower Grenville crust during or after the orogenic phases. A thicker crust beneath these regions is also coincident with a thicker Moho interface (Figure S17, supporting information) which can be explained by underplating processes (Petrescu et al., 2016).

Comparing the shear velocity profiles perpendicular to the trend of the Appalachian tectonic domains along different part of the orogen (Figure 10), it becomes clear that the 3D seismic structure of the northern Appalachian crust is very complex and more variable than that observed beneath the Grenville and the eastern Superior. Previous seis-

mic studies also mentioned a more complex Appalachian crust than the older tectonic provinces in eastern Canada as suggested by their Moho depth and Poisson's ratio variations (e.g., Levin et al., 2017; Petrescu et al., 2016; Darbyshire et al., 2017). Results from this study suggest changes of seismic signatures including crustal thickness, Moho thickness, and relative thickness of upper and lower crustal layers over a relatively short distance due to the diverse nature of tectonic events that resulted in the assembly of the Appalachians.

A variable seismic structure of the crust within the Taconic terranes of the northern Appalachians provides evidence for at least two different metamorphism episodes with different characteristics that occured during the Early Paleozoic Taconic orogeny. Beneath the St. Lawrence rifting system and the Humber margin, upper and middle crust under the first sedimentary layer is generally faster than its surroundings in the Appalachians and the Grenville in our shear velocity model (Figure S14, supporting information). This region also coincides with high Vp/Vs ratios indicating a high mafic content (Petrescu et al., 2016). It is possible that rift-related tectonics after break-up of Rodinia not only resulted in development of a relatively thick sedimentary basin, but it also created a zone of weakness in the crust acting as a stress guide for magma material which modified the composition of the crust beneath these regions. The observed higher velocity upper crust beneath these areas may be a result of different accretional/collisional processes that occured in the evolution of the northern Appalachians during the Taconic orogeny. Accretion of the Humber margin to Laurentia was different in terms of rheological coupling between the upper and lower plates than the later arriving Peri-Laurentian terranes (i.e., Dashwoods, C. van Staal & Zagorevski, 2020). Deformation was limited to underthrusted Humber margin manifested in low grade metamorphism and structurally intact suprasubduction-zone ophiolites, whereas the adjacent Dashwoods block is dominated by strongly metamorphosed and deformed sedimentary rocks of various ages and arc ophiolites (C. van Staal & Zagorevski, 2020, and references therein). Accordingly, we suggest that the short scale variations of seismic velocities within the Peri-Laurentian terranes of the Appalachians are mostly compositional and preserve evidence for variable degree of metamorphism at distinct accretionary/collisional episodes of the Taconic orogeny.

As suggested by our tomographic models (Figures 8-9), crustal structure of the Salinic terranes (i.e., Ganderia) is seismically slower and generally different than that of the later

arriving Peri-Gondwanan terranes (i.e., Avalonia and Meguma). Ganderia's rifting from West Gondwana, its drift across the Iapetus ocean, and its accretion to Laurentia were independent from the Avalonia and Meguma terranes (C. R. van Staal et al., 2021). Hence after the onset of the Paleozoic, Ganderia and Avalonia were two different unrelated terranes (C. R. van Staal et al., 2009). As opposed to Ganderia, Avalonia was not involved in the Appalachian accretionary events untill the Late Silurian (C. R. van Staal & Barr, 2012), and the observed differences of the seismic charactristics may be due to their different tectonic histories in the Early Paleozoic in terms within-plate magmatism and metamorphism en route to Laurentia (C. R. van Staal et al., 2012). A lack of significant difference for the crustal seismic signatures of Avalonia and Meguma may also suggest that Avalonia and Meguma were never separated by a wide ocean basin. It is also likely that they were only separated by extended continental crust rather than an oceanic basin until they collided during the Neo-Acadian orogeny. This interpretation is also compatible with the observed relatively thick crust beneath the pertinent terranes.

6 Conclusions

Using more than two years of ambient seismic noise data recorded by relatively dense arrays of broadband seismograph stations, we took the most detailed look at the seismic structure of the crust beneath SE Canada and the NE USA to date. Our Rayleigh wave tomographic models enabled us to discuss the observed variations in the azimuthal anisotropy, the crustal velocities, and the Moho depth and thickness in terms of their tectonic implications. The azimuthal anisotropy is oriented mainly along the general tectonic trend (i.e., NE-SW), but localized variations of seismic anisotropy are observed beneath the Bay of Fundy and across the Appalachian structral front. The Precambrian tectonic provinces, namely the Grenville and the Superior, are generally dominated by fast seismic velocities, whereas prominent slow velocity regions are observed beneath different regions in the Appalachians. Relatively thick sedimentary layers are observed beneath the Gulf of St. Lawrence, the St. Lawrence river, Bay of Fundy, and under the St. Lawrence Platform with their thicknesses interpreted to be 8-10 km, 5-6 km, 3-4 km, 1-2 km respectively. Using shear velocity proxies, we estimated Moho depth and thickness across the study area. Crustal thickness in the study area is highly variable, ranging from ~32 to 52 km. Regions with the deepest Moho are found beneath the Grenville Province, whereas the shallowest Moho areas are beneath the Gulf of Maine and the Gulf

947 of St. Lawrence in the Appalachians. A thicker crust and Moho interface in the Grenville

948 Province could be explained by underplating processes. A NE-SW trending Moho off-

949 set feature in the central northern Appalachians is interpreted as the boundary between

950 the Peri-Laurentian and Peri-Gondwanan terranes at depth. Variations of seismic sig-

951 nature within the westernmost terranes of the Applachians (i.e., the Taconic terranes)

952 provide evidence for at least two episodes of metamorphism in the Peri-Laurentian zones

953 of the northern Appalachians. We observe very similar seismic signatures for Avalonia

954 and Meguma, whereas the seismic velocities in the Peri-Gondwanan tectonic domains

955 of Ganderia and Avalonia are notably different. Ganderia crust is generally seismically

956 slow, whereas the post-Acadian domains of Avalonia and Meguma are dominated by fast

957 velocities, and their similar seismic signatures could suggest a different tectonic history

958 in terms of their within-plate magmatism and metamorphism than Ganderia terranes

959 en route to Laurentia in the Early Paleozoic. Similar seismic signatures observed for Aval-

960 onia and Meguma, especially at mid-to-lower crustal depths, may suggest that they were

961 originally separated by either a narrow ocean basin or by extended continental crust.

References

Afonso, J., Fullea, J., Griffin, W., Yang, Y., Jones, A., D. Connolly, J., & O'Reilly, S. (2013). 3-D multiobservable probabilistic inversion for the compositional and thermal structure of the lithosphere and upper mantle. I: A priori petrological information and geophysical observables. *Journal of Geophysical Research: Solid Earth*, *118*(5), 2586–2617. doi: 10.1002/jgrb.50124

Amante, C., & Eakins, B. W. (2009). *ETOPO1 arc-minute global relief model: procedures, data sources and analysis.* doi: 10.7289/V5C8276M

ASL, A. S. L. A.-U. (1994). *New England Seismic Network.* International Federation of Digital Seismograph Networks. Dataset/Seismic Network. doi: 10.7914/SN/NE

Bagherpur Mojaver, O., Darbyshire, F., & Dave, R. (2021). Lithospheric Structure and Flat-Slab Subduction in the Northern Appalachians: Evidence From Rayleigh Wave Tomography. *Journal of Geophysical Research: Solid Earth*, *126*(4), e2020JB020924. doi: 10.1029/2020JB020924

Bensen, G., Ritzwoller, M., Barmin, M., Levshin, A. L., Lin, F., Moschetti, M., ... Yang, Y. (2007). Processing seismic ambient noise data to obtain reliable broadband surface wave dispersion measurements. *Geophysical Journal International*, *169*(3), 1239–1260. doi: 10.1111/j.1365-246X.2007.03374.x

Bensen, G., Ritzwoller, M., & Shapiro, N. M. (2008). Broadband ambient noise surface wave tomography across the United States. *Journal of Geophysical Research: Solid Earth*, *113*(B5). doi: 10.1029/2007JB005248

Bensen, G., Ritzwoller, M., & Yang, Y. (2009). A 3-D shear velocity model of the crust and uppermost mantle beneath the United States from ambient seismic noise. *Geophysical Journal International*, *177*(3), 1177–1196. doi: 10.1111/j.1365-246X.2009.04125.x

Boyce, A., Bastow, I., Darbyshire, F. A., Ellwood, A., Gilligan, A., Levin, V., & Menke, W. (2016). Subduction beneath Laurentia modified the eastern North American cratonic edge: Evidence from P wave and S wave tomography. *Journal of Geophysical Research: Solid Earth*, *121*(7), 5013–5030. doi: 10.1002/2016JB012838

Brown, M. (2010). Melting of the continental crust during orogenesis: the thermal, rheological, and compositional consequences of melt transport from lower to up-

per continental crust. *Canadian Journal of Earth Sciences*, *47*(5), 655–694. doi: 10.1139/E09-057

Carr, S., Easton, R., Jamieson, R. A., & Culshaw, N. (2000). Geologic transect across the Grenville orogen of Ontario and New York. *Canadian Journal of Earth Sciences*, *37*(2-3), 193–216. doi: 10.1139/e99-074

Clouzet, P., Masson, Y., & Romanowicz, B. (2018). Box tomography: first application to the imaging of upper-mantle shear velocity and radial anisotropy structure beneath the North American continent. *Geophysical Journal International*, *213*(3), 1849–1875. doi: 10.1093/gji/ggy078

Clowes, R. M. (2010). Initiation, development, and benefits of Lithoprobe—shaping the direction of Earth science research in Canada and beyond. *Canadian Journal of Earth Sciences*, *47*(4), 291–314.

Cook, F. A., White, D. J., Jones, A. G., Eaton, D. W., Hall, J., & Clowes, R. M. (2010). How the crust meets the mantle: Lithoprobe perspectives on the Mohorovičić discontinuity and crust–mantle transition. *Canadian Journal of Earth Sciences*, *47*(4), 315–351. doi: 10.1139/E09-076

Darbyshire, F. A., Bastow, I., Forte, A., Hobbs, T., Calvel, A., Gonzalez-Monteza, A., & Schow, B. (2015). Variability and origin of seismic anisotropy across eastern Canada: Evidence from shear wave splitting measurements. *Journal of Geophysical Research: Solid Earth*, *120*(12), 8404–8421. doi: 10.1002/2015JB012228

Darbyshire, F. A., Bastow, I., Petrescu, L., Gilligan, A., & Thompson, D. (2017). A tale of two orogens: Crustal processes in the Proterozoic Trans-Hudson and Grenville Orogens, eastern Canada. *Tectonics*, *36*(8), 1633–1659. doi: 10.1002/2017TC004479

Darbyshire, F. A., Dahl-Jensen, T., Larsen, T. B., Voss, P. H., & Joyal, G. (2018). Crust and uppermost-mantle structure of Greenland and the Northwest Atlantic from Rayleigh wave group velocity tomography. *Geophysical Journal International*, *212*(3), 1546–1569. doi: 10.1093/gji/ggx479

Darbyshire, F. A., & Lebedev, S. (2009). Rayleigh wave phase-velocity heterogeneity and multilayered azimuthal anisotropy of the Superior Craton, Ontario. *Geophysical Journal International*, *176*(1), 215–234. doi: 10.1111/j.1365-246X.2008.03982.x

Debayle, E., & Kennett, B. (2000). The Australian continental upper mantle:

structure and deformation inferred from surface waves. *Journal of Geophysical Research: Solid Earth*, *105*(B11), 25423–25450. doi: 10.1029/2000JB900212

Deschamps, F., Lebedev, S., Meier, T., & Trampert, J. (2008). Azimuthal anisotropy of Rayleigh-wave phase velocities in the east-central United States. *Geophysical Journal International*, *173*(3), 827–843. doi: 10.1111/j.1365-246X.2008.03751.x

Eaton, D., Adams, J., Asudeh, I., Atkinson, G., Bostock, M., Cassidy, J., . . . Unsworth, M. (2005). Investigating Canada's lithosphere and earthquake hazards with portable arrays. *EOS Transactions of the American Geophysical Union*, *86*, 169, 173. doi: 10.1029/eost2005EO17

Ekström, G., Abers, G. A., & Webb, S. C. (2009). Determination of surface-wave phase velocities across USArray from noise and Aki's spectral formulation. *Geophysical Research Letters*, *36*(18). doi: 10.1029/2009GL039131

Foster, A., Darbyshire, F., & Schaeffer, A. (2020). Anisotropic structure of the central North American Craton surrounding the Mid-Continent Rift: evidence from Rayleigh waves. *Precambrian Research*, *342*, 105662. doi: 10.1016/j.precamres.2020.105662

Fountain, D. M., & Christensen, N. I. (1989). Composition of the continental crust and upper mantle: A review. *Geophysical Framework of the Continental United States*, *172*, 711–742.

Funck, T., Jackson, H. R., Louden, K. E., Dehler, S. A., & Wu, Y. (2004). Crustal structure of the northern Nova Scotia rifted continental margin (eastern Canada). *Journal of Geophysical Research: Solid Earth*, *109*(B9). doi: 10.1029/2004JB003008

Geological Survey of Canada. (1989). *Canadian National Seismograph Network.* International Federation of Digital Seismograph Networks. Dataset/Seismic Network. doi: 10.7914/SN/CN

Gilligan, A., Bastow, I. D., Watson, E., Darbyshire, F. A., Levin, V., Menke, W., . . . others (2016). Lithospheric deformation in the Canadian Appalachians: evidence from shear wave splitting. *Geophysical Journal International*, *206*(2), 1273–1280. doi: 10.1093/gji/ggw207

Golos, E., Fang, H., Yao, H., Zhang, H., Burdick, S., Vernon, F., . . . Van der Hilst, R. (2018). Shear wave tomography beneath the United States using a joint inversion of surface and body waves. *Journal of Geophysical Research: Solid Earth*,

1077   *123*(6), 5169–5189. doi: 10.1029/2017JB014894

1078 Green, R. G., Priestley, K. F., & White, R. S. (2017). Ambient noise tomography

1079   reveals upper crustal structure of Icelandic rifts. *Earth and Planetary Science Let-*

1080   *ters*, *466*, 20–31. doi: 10.1016/j.epsl.2017.02.039

1081 Guo, Z., Chen, Y. J., Ning, J., Yang, Y., Afonso, J. C., & Tang, Y. (2016). Seismic

1082   evidence of on-going sublithosphere upper mantle convection for intra-plate vol-

1083   canism in Northeast China. *Earth and Planetary Science Letters*, *433*, 31–43. doi:

1084   10.1016/j.epsl.2015.09.035

1085 Hall, J., Marillier, F., & Dehler, S. (1998). Geophysical studies of the structure of

1086   the appalachian orogen in the atlantic borderlands of canada. *Canadian Journal*

1087   *of Earth Sciences*, *35*(11), 1205–1221.

1088 Hammer, P. T., Clowes, R. M., Cook, F. A., van der Velden, A. J., & Vasudevan, K.

1089   (2010). The Lithoprobe trans-continental lithospheric cross sections: imaging the

1090   internal structure of the North American continent. *Canadian Journal of Earth*

1091   *Sciences*, *47*(5), 821–857. doi: 10.1139/E10-036

1092 Hibbard, J. P., van Staal, C. R., & Miller, B. V. (2007). Links among Carolinia,

1093   Avalonia, and Ganderia in the Appalachian peri-Gondwanan realm. *Geological So-*

1094   *ciety of America Special Papers*, *433*, 291–311. doi: 10.1130/2007.2433(14)

1095 Hibbard, J. P., van Staal, C. R., & Rankin, D. W. (2007). A comparative analysis of

1096   pre-Silurian crustal building blocks of the northern and the southern Appalachian

1097   orogen. *American Journal of Science*, *307*(1), 23–45. doi: 10.2475/01.2007.02

1098 Hughes, S., & Luetgert, J. H. (1991). Crustal structure of the western new england

1099   appalachians and the adirondack mountains. *Journal of Geophysical Research:*

1100   *Solid Earth*, *96*(B10), 16471–16494.

1101 Hunter, J. D. (2007). Matplotlib: A 2D graphics environment. *Computing in Science*

1102   *& Engineering*, *9*(3), 90–95. doi: 10.1109/MCSE.2007.55

1103 Hynes, A., & Rivers, T. (2010). Protracted continental collision—Evidence from the

1104   Grenville orogen. *Canadian Journal of Earth Sciences*, *47*(5), 591–620. doi: 10

1105   .1139/E10-003

1106 IRIS Transportable Array. (2003). *USArray Transportable Array.* International Fed-

1107   eration of Digital Seismograph Networks. Dataset/Seismic Network. doi: 10.7914/

1108   SN/TA

1109 Kamo, S., Krogh, T., & Kumarapeli, P. (1995). Age of the Grenville dyke swarm,

Ontario-Quebec: implications for the timing of Iapetan rifting. *Canadian Journal of Earth Sciences*, *32*(3), 273–280. doi: 10.1139/e95-022

Kamo, S. L., Gower, C. F., & Krogh, T. E. (1989). Birthdate for the Iapetus Ocean? A precise U-Pb zircon and baddeleyite age for the Long Range dikes, southeast Labrador. *Geology*, *17*(7), 602–605. doi: 10.1130/0091-7613(1989)017⟨0602: BFTLOA⟩2.3.CO;2

Kao, H., Behr, Y., Currie, C. A., Hyndman, R., Townend, J., Lin, F.-C., ... He, J. (2013). Ambient seismic noise tomography of Canada and adjacent regions: Part I. Crustal structures. *Journal of Geophysical Research: Solid Earth*, *118*(11), 5865–5887. doi: 10.1002/2013JB010535

Kennett, B. L., Engdahl, E., & Buland, R. (1995). Constraints on seismic velocities in the Earth from traveltimes. *Geophysical Journal International*, *122*(1), 108–124. doi: 10.1111/j.1365-246X.1995.tb03540.x

Köhler, A., Weidle, C., & Maupin, V. (2011). Directionality analysis and Rayleigh wave tomography of ambient seismic noise in southern Norway. *Geophysical Journal International*, *184*(1), 287–300. doi: 10.1111/j.1365-246X.2010.04830.x

Kuponiyi, A. P., Kao, H., van Staal, C. R., Dosso, S. E., Cassidy, J. F., & Spence, G. D. (2017). Upper crustal investigation of the Gulf of Saint Lawrence region, eastern Canada using ambient noise tomography. *Journal of Geophysical Research: Solid Earth*, *122*(7), 5208–5227. doi: 10.1002/2016JB013865

Levin, V., Servali, A., Van Tongeren, J., Menke, W., & Darbyshire, F. A. (2017). Crust-mantle boundary in eastern North America, from the (oldest) craton to the (youngest) rift. *Geological Society of America Special Paper*, *526*, 107–131. doi: 10.1130/2017.2526(06)

Li, C., Gao, H., & Williams, M. L. (2020). Seismic characteristics of the eastern North American crust with Ps converted waves: Terrane accretion and modification of continental crust. *Journal of Geophysical Research: Solid Earth*, *125*(5), e2019JB018727. doi: 10.1029/2019JB018727

Li, C., Gao, H., Williams, M. L., & Levin, V. (2018). Crustal thickness variation in the northern Appalachian Mountains: Implications for the geometry of 3-D tectonic boundaries within the crust. *Geophysical Research Letters*, *45*(12), 6061–6070. doi: 10.1029/2018GL078777

Lin, F.-C., Moschetti, M. P., & Ritzwoller, M. H. (2008). Surface wave tomography

of the western United States from ambient seismic noise: Rayleigh and Love wave phase velocity maps. *Geophysical Journal International*, *173*(1), 281–298. doi: 10.1111/j.1365-246X.2008.03720.x

Long, M. D., Jackson, K. G., & McNamara, J. F. (2016). SKS splitting beneath T ransportable A rray stations in eastern N orth A merica and the signature of past lithospheric deformation. *Geochemistry, Geophysics, Geosystems*, *17*(1), 2–15. doi: 10.1002/2015GC006088

Ludden, J., & Hynes, A. (2000). The Lithoprobe Abitibi-Grenville transect: two billion years of crust formation and recycling in the Precambrian Shield of Canada. *Canadian Journal of Earth Sciences*, *37*(2-3), 459–476. doi: 10.1139/e99-120

Macdonald, F., Ryan-Davis, J., Coish, R., Crowley, J., & Karabinos, P. (2014). A newly identified Gondwanan terrane in the Northern Appalachian Mountains: Implications for the Taconic orogeny and closure of the Iapetus Ocean. *Geology*, *42*(6), 539–542. doi: 10.1130/G35659.1

Martignole, J., & Calvert, A. (1996). Crustal-scale shortening and extension across the Grenville province of western Quebec. *Tectonics*, *15*(2), 376–386. doi: 10.1029/95TC03748

McLellan, M., Schaeffer, A. J., & Audet, P. (2018). Structure and fabric of the crust and uppermost mantle in the northern Canadian Cordillera from Rayleigh-wave tomography. *Tectonophysics*, *724*, 28–41. doi: 10.1016/j.tecto.2018.01.011

Menke, W., Levin, V., & Darbyshire, F. A. (2012). *Deep Structure of Three Continental Sutures in Eastern North America (QM-III).* International Federation of Digital Seismograph Networks; Dataset/Seismic network. doi: 10.7914/SN/X8_2012

Menke, W., Skryzalin, P., Levin, V., Harper, T., Darbyshire, F. A., & Dong, T. (2016). The Northern Appalachian Anomaly: A modern asthenospheric upwelling. *Geophysical Research Letters*, *43*(19), 173–179. doi: 10.1002/2016GL070918

Musacchio, G., Mooney, W. D., Luetgert, J. H., & Christensen, N. I. (1997). Composition of the crust in the Grenville and Appalachian Provinces of North America inferred from Vp/Vs ratios. *Journal of Geophysical Research: Solid Earth*, *102*(B7), 15225–15241. doi: 10.1029/96JB03737

Pawlak, A., Eaton, D. W., Darbyshire, F., Lebedev, S., & Bastow, I. D. (2012). Crustal anisotropy beneath Hudson Bay from ambient noise tomography: Evi-

dence for post-orogenic lower-crustal flow? *Journal of Geophysical Research: Solid Earth*, *117*(B8). doi: 10.1029/2011JB009066

Petrescu, L., Bastow, I., Darbyshire, F. A., Gilligan, A., Bodin, T., Menke, W., & Levin, V. (2016). Three billion years of crustal evolution in eastern Canada: Constraints from receiver functions. *Journal of Geophysical Research: Solid Earth*, *121*(2), 788–811. doi: 10.1002/2015JB012348

Petrescu, L., Darbyshire, F. A., Bastow, I., Totten, E., & Gilligan, A. (2017). Seismic anisotropy of Precambrian lithosphere: Insights from Rayleigh wave tomography of the eastern Superior Craton. *Journal of Geophysical Research: Solid Earth*, *122*(5), 3754–3775. doi: 10.1002/2016JB013599

Prieto, G., Lawrence, J., & Beroza, G. (2009). Anelastic Earth structure from the coherency of the ambient seismic field. *Journal of Geophysical Research: Solid Earth*, *114*(B7). doi: 10.1029/2008JB006067

Ritsema, J., & Lekić, V. (2020). Heterogeneity of seismic wave velocity in Earth's mantle. *Annual Review of Earth and Planetary Sciences*, *48*, 377–401. doi: 10.1146/annurev-earth-082119-065909

Rivers, T. (1997). Lithotectonic elements of the grenville province: review and tectonic implications. *Precambrian Research*, *86*(3-4), 117–154. doi: 10.1016/S0301-9268(97)00038-7

Rivers, T. (2008). Assembly and preservation of lower, mid, and upper orogenic crust in the Grenville Province—Implications for the evolution of large hot long-duration orogens. *Precambrian Research*, *167*(3-4), 237–259. doi: 10.1016/j.precamres.2008.08.005

Rivers, T. (2015). Tectonic Setting and Evolution of the Grenville Orogen: An Assessment of Progress Over the Last 40 Years. *Geoscience Canada*, *42*(1). doi: 10.12789/geocanj.2014.41.057

Rivers, T., Ketchum, J., Indares, A., & Hynes, A. (2002). The high pressure belt in the grenville province: architecture, timing, and exhumation. *Canadian Journal of Earth Sciences*, *39*(5), 867–893. doi: 10.1139/e02-025

Rivers, T., Martignole, J., Gower, C., & Davidson, A. (1989). New tectonic divisions of the Grenville Province, southeast Canadian Shield. *Tectonics*, *8*(1), 63–84. doi: 10.1029/TC008i001p00063

Sadeghisorkhani, H., Gudmundsson, Ó., & Tryggvason, A. (2018). GSpecDisp:

A matlab GUI package for phase-velocity dispersion measurements from ambient-noise correlations. *Computers & Geosciences*, *110*, 41–53. doi: 10.1016/j.cageo.2017.09.006

Schaeffer, A., & Lebedev, S. (2013). Global shear speed structure of the upper mantle and transition zone. *Geophysical Journal International*, *194*(1), 417–449. doi: 10.1093/gji/ggt095

Schaeffer, A., & Lebedev, S. (2014). Imaging the North American continent using waveform inversion of global and USArray data. *Earth and Planetary Science Letters*, *402*, 26–41. doi: 10.1016/j.epsl.2014.05.014

SEIS-UK. (2013). *QM-III Network - Atlantic Canada.* International Federation of Digital Seismograph Networks; Dataset/Seismic network.

Shapiro, N. M., & Campillo, M. (2004). Emergence of broadband Rayleigh waves from correlations of the ambient seismic noise. *Geophysical Research Letters*, *31*(7). doi: 10.1029/2004GL019491

Shapiro, N. M., Campillo, M., Stehly, L., & Ritzwoller, M. H. (2005). High-resolution surface-wave tomography from ambient seismic noise. *Science*, *307*(5715), 1615–1618. doi: 10.1126/science.1108339

Shen, W., & Ritzwoller, M. H. (2016). Crustal and uppermost mantle structure beneath the United States. *Journal of Geophysical Research: Solid Earth*, *121*(6), 4306–4342. doi: 10.1002/2016JB012887

Smith, M. L., & Dahlen, F. (1973). The azimuthal dependence of Love and Rayleigh wave propagation in a slightly anisotropic medium. *Journal of Geophysical Research*, *78*(17), 3321–3333. doi: 10.1029/JB078i017p03321

Stockmal, G., Colman-Sadd, S., Keen, C., O'Brien, S., & Quinlan, G. (1987). Collision along an irregular margin: a regional plate tectonic interpretation of the Canadian Appalachians. *Canadian Journal of Earth Sciences*, *24*(6), 1098–1107. doi: 10.1139/e87-107

Tarantola, A. (2005). *Inverse problem theory and methods for model parameter estimation.* SIAM.

Tian, Y., & Ritzwoller, M. H. (2015). Directionality of ambient noise on the Juan de Fuca plate: Implications for source locations of the primary and secondary microseisms. *Geophysical Journal International*, *201*(1), 429–443. doi: 10.1093/gji/ggv024

van der Lee, S., & Frederiksen, A. (2005). Surface wave tomography applied to the North American upper mantle. *Seismic Earth: Array analysis of broadband seismograms*, *157*, 67–80. doi: 10.1029/157GM05

van Staal, C., & Zagorevski, A. (2020). Accretion, Soft and Hard Collision: Similarities, Differences and an Application from the Newfoundland Appalachian Orogen. *Geoscience Canada: Journal of the Geological Association of Canada/Geoscience Canada: journal de l'Association Géologique du Canada*, *47*(3), 103–118. doi: 10.12789/geocanj.2020.47.161

van Staal, C. R., & Barr, S. (2012, 01). Lithospheric architecture and tectonic evolution of the Canadian Appalachians and associated Atlantic margin. *Geological Association of Canada, Special Paper*, *49*, 41–95.

van Staal, C. R., Barr, S. M., & Murphy, J. B. (2012). Provenance and tectonic evolution of Ganderia: Constraints on the evolution of the Iapetus and Rheic oceans. *Geology*, *40*(11), 987–990. doi: 10.1130/G33302.1

van Staal, C. R., Barr, S. M., Waldron, J. W., Schofield, D. I., Zagorevski, A., & White, C. E. (2021). Provenance and Paleozoic tectonic evolution of Ganderia and its relationships with Avalonia and Megumia in the Appalachian-Caledonide orogen. *Gondwana Research*, *98*, 212–243. doi: 10.1016/j.gr.2021.05.025

van Staal, C. R., Whalen, J. B., Valverde-Vaquero, P., Zagorevski, A., & Rogers, N. (2009). Pre-Carboniferous, episodic accretion-related, orogenesis along the Laurentian margin of the northern Appalachians. *Geological Society, London, Special Publications*, *327*(1), 271–316. doi: 10.1144/SP327.13

Villemaire, M., Darbyshire, F. A., & Bastow, I. (2012). P-wave tomography of eastern North America: Evidence for mantle evolution from Archean to Phanerozoic, and modification during subsequent hot spot tectonism. *Journal of Geophysical Research: Solid Earth*, *117*(B12). doi: 10.1029/2012JB009639

Wessel, P., Smith, W. H., Scharroo, R., Luis, J., & Wobbe, F. (2013). Generic mapping tools: improved version released. *EOS, Transactions American Geophysical Union*, *94*(45), 409–410. doi: 10.1002/2013EO450001

Whitmeyer, S. J., & Karlstrom, K. E. (2007). Tectonic model for the Proterozoic growth of North America. *Geosphere*, *3*(4), 220–259. doi: 10.1130/GES00055.1

Williams, H., Colman-Sadd, S., & Swinden, H. (1988). Tectonic-stratigraphic subdivisions of central Newfoundland. *Current Research, Part B. Geological Survey of*

1275   *Canada, Paper*, *88*, 91–98. doi: 10.4095/122414

1276 Wilson, R. A., van Staal, C. R., & Kamo, S. L.   (2017).   Rapid transition from the

1277   Salinic to Acadian orogenic cycles in the northern Appalachian Orogen: Evidence

1278   from northern New Brunswick, Canada.   *American Journal of Science*, *317*(4),

1279   449–482. doi: 10.2475/04.2017.02

1280 Withjack, M. O., Olsen, P. E., & Schlische, R. W.   (1995).   Tectonic evolution of

1281   the Fundy rift basin, Canada: evidence of extension and shortening during passive

1282   margin development. *Tectonics*, *14*(2), 390–405. doi: 10.1029/94TC03087

1283 Withjack, M. O., Schlische, R. W., & Baum, M. S. (2009). Extensional development

1284   of the Fundy rift basin, southeastern Canada. *Geological Journal*, *44*(6), 631–651.

1285   doi: 10.1002/gj.1186

1286 Yang, B. B., Liu, Y., Dahm, H., Liu, K. H., & Gao, S. S.   (2017).   Seismic azimuthal

1287   anisotropy beneath the eastern United States and its geodynamic implications.

1288   *Geophysical Research Letters*, *44*(6), 2670–2678. doi: 10.1002/2016GL071227

1289 Yang, Y., Li, A., & Ritzwoller, M. H.   (2008).   Crustal and uppermost man-

1290   tle structure in southern Africa revealed from ambient noise and teleseis-

1291   mic tomography.   *Geophysical Journal International*, *174*(1), 235–248.   doi:

1292   10.1111/j.1365-246X.2008.03779.x

1293 Yang, Y., Ritzwoller, M. H., Levshin, A. L., & Shapiro, N. M. (2007). Ambient noise

1294   Rayleigh wave tomography across Europe.   *Geophysical Journal International*,

1295   *168*(1), 259–274. doi: 10.1111/j.1365-246X.2006.03203.x

1296 Yao, H., van Der Hilst, R. D., & De Hoop, M. V.   (2006).   Surface-wave array to-

1297   mography in SE Tibet from ambient seismic noise and two-station analysis—I.

1298   Phase velocity maps.   *Geophysical Journal International*, *166*(2), 732–744.   doi:

1299   10.1111/j.1365-246X.2006.03028.x

1300 Yuan, H., French, S., Cupillard, P., & Romanowicz, B.   (2014).   Lithospheric ex-

1301   pression of geological units in central and eastern North America from full wave-

1302   form tomography.   *Earth and Planetary Science Letters*, *402*, 176–186.   doi:

1303   10.1016/j.epsl.2013.11.057